Estuarine, Coastal and Shelf Science 281 (2023) 108212

Contents lists available at ScienceDirect

Estuarine, Coastal and Shelf Science

journal homepage: www elsevier com/locate/ecss

Modelled coastal circulation and Lagrangian statistics from a large coastal embayment: The case of Bay of Plenty, Aotearoa New Zealand

Mireya M. Montaño [a,*], Sutara H. Suanda [b], João Marcos Azevedo Correia de Souza [c]

[a] University of Otago Department of Marine Science Dunedin 9010 Otago New Zealand
[b] University of North Carolina at Wilmington Department of Physics and Physical Oceanography 28403 NC United States
[c] MetOcean Solutions a division of MetService of New Zealand Raglan 3225 Waikato New Zealand

ARTICLE INFO

Keywords:
Model evaluation
Lagrangian statistics
Coastal upwelling
Embayment circulation

ABSTRACT

In this study, a high-resolution one-way nested, hindcast ROMS model was developed to analyse the coastal circulation and Lagrangian statistics within the Bay of Plenty (BoP) region in Aotearoa, New Zealand. The Bay of Plenty Model (BoPM) was statistically evaluated against a set of multiple remote sensing and in situ observations from 2003–2004, forming the analysis period for this study. Overall, the BoPM possesses good skill reproducing ocean water temperature, salinity, sea level and water column velocity over tidal and non-tidal timescales (Willmott skill >0.8 for most variables). Root-mean-squared errors of <1 °C for ocean water temperature, ≈0.15 for salinity (an exception present during winter), <8 cm s^{-1} for water column velocity and 0.09 m for non-tidal sea surface height are achieved. Over the 2-year period, nearshore modelled sea surface currents are correlated to local wind forcing on the western and central region of the BoP consistent with coastal wind-driven upwelling dynamics. Up to 30 of the cross-shelf current variability is explained by along-shore wind stress, consistent with previous observational studies. Meanwhile, the eastern region has no significant correlation to the along-shore winds, suggesting other forcings must be considered. Circulation patterns and Lagrangian statistics under two distinct atmospheric conditions over the two years were analysed: January, with predominantly moderate upwelling-favourable winds and July, with highly variable and stronger winds. January conditions show an eastward flowing large-scale boundary current, the East Auckland Current (EAUC), and a quasi-stationary eddy, the East Cape Eddy (ECE), close to the shelf break, while July conditions show the EAUC and ECE located further from shore. A series of particle release experiments from inner-, mid-shelf, and shelf break locations are used to identify trajectory and dispersion variability between western, central, and eastern sections of the BoP under January and July conditions. Particles released under January conditions tend to flow eastward following the EAUC. Under July conditions, inner- and mid-shelf releases converge towards the central BoP, where bathymetric changes and islands create pathways for particles to exit the continental shelf. Relative dispersion (R^2) under January conditions shows a ballistic dispersion regime ($R^2 \approx t^2$) over the first 10 days followed by a diffusive regime ($R^2 \approx t^1$) after 15 days. Under July conditions, a ballistic-like regime is maintained throughout a 30-day period, likely due to strong mixing in the BoP associated with submesoscale processes. Particles released in proximity to East Cape headland that remain in the water column for > 5 days show higher dispersion relative to releases from the central and western regions of the BoP. However, 70 –90 of particles released on the eastern inner-shelf strand to the coastline in <5 days. This suggests that the eastern region can act as a retention zone, constraining the particles towards the shore. Drift duration increases for particles released further from the shore, where offshore mesoscale currents influence them more, and islands become important receptor locations.

1. Introduction

Understanding the drivers and variability of near-shore coastal circulation is essential to improve the management of human activities such as open ocean aquaculture, fishing tourism, navigation, and pollution. This need is rising as coastal systems respond to climate change and additional increasing anthropogenic pressures. Although sustained ocean observations and monitoring provide the foundation for many coastal circulation studies (i.e., Heath, 1985; Roughan

* Corresponding author.
E-mail address: mireya.mmor@gmail.com (M.M. Montaño).

https://doi.org/10.1016/j.ecss.2023.108212
Received 16 July 2022; Received in revised form 21 December 2022; Accepted 3 January 2023
Available online 5 January 2023

et al., 2015; Stevens et al., 2021), realistic, long-running and evaluated oceanic numerical simulations can also provide information about coastal dynamics at a spatial and temporal resolution that is difficult to collect from observations alone (i.e., Wilkin, 2006; Zhang et al., 2019; Hauri et al., 2020; Souza et al., 2022). To be most useful, numerical simulations are often first evaluated against available in situ and satellite observations. An objective assessment of model performance is given by a series of statistical metrics that quantify the difference between the model and observations. (i.e. Mean Bias, Mean-square error, and others, see Section 2.2). Once confidence in a numerical model is demonstrated, it can become one powerful tool for coastal managers that offers gap-free information on water quality, properties and hydrodynamics, providing the chance to experiment with alterations to the coastal system and even offer predictive capabilities (i.e., Mitarai et al., 2009; Jones et al., 2016; Elliot et al., 2021).

Since 2018, efforts have been made in Aotearoa, New Zealand, to provide gap-free information about the ocean state as part of the Moana Project. This national project aims to improve the understanding of the surrounding ocean dynamics (i.e., circulation, connectivity, marine heatwaves) to provide information that supports Aotearoa New Zealand's seafood industry (for more information, visit www.moanaproject.org). Due to the extensive territorial sea, complex bathymetry, and interaction between basin O(>100 km) and mesoscale O(10–100 km) dynamics that Aotearoa New Zealand possesses, a well-evaluated regional circulation model is a helpful tool to study the surrounding oceans. Within the Moana Project framework, a 28-year regional hindcast (≈5 km horizontal resolution) was developed (Souza, 2022). The long-running model is based on the Regional Ocean Modelling System (ROMS) to better understand oceanic variability, long-term trends and extreme events around Aotearoa, New Zealand. This simulation was done using realistic atmospheric, tidal and boundary forcing and can represent relevant ocean processes (i.e., boundary currents, mesoscale eddies, marine heat waves) (Souza et al., 2022). This particular model is briefly described below as it serves as the parent model for this current study.

A common issue with regional-scale numerical models is that they do not resolve local coastal scales (≤10 km). As a result, local circulation models (typically ≤1 km horizontal resolution) have been developed to study local coastal dynamics. Similar to regional circulation models that consider basin- and mesoscale dynamics, local circulation models take into consideration mesoscale O(10–100 km) and submesoscale O(<10 km) dynamics. Therefore, local circulation models can simulate a realistic coastal system if regional and local forcings (i.e. bay-shelf exchange, river influence, local winds, island wakes) and realistic coastal features (i.e. high-resolution bathymetry, more defined coastline) are represented (Zhang et al., 2019; Kärnä et al., 2015; Goubanova et al., 2019; Myksvoll et al., 2012; Dong and McWilliams, 2007). Short-term local circulation models have been developed across Aotearoa, New Zealand, to address specific issues. For the Cook Strait, a body of water with high levels of turbulence, a 3-year local circulation model was used to estimate the volume flux between the north and south islands of New Zealand (Hadfield and Stevens, 2021). For the Bay of Plenty, a 30-day local circulation model was used to estimate the dispersal patterns of the Rena Oil Spill (Jones et al., 2016).

To improve emergency response and management practices, from event-scale situations such as an oil spill (e.g., Beron-Vera and LaCasce, 2016; Jones et al., 2016) to the seasonal-scale such as the study of larvae dispersal (e.g., Cowen et al., 2006; Chiswell and Rickard, 2011; Norrie et al., 2020), it is necessary to understand water parcel movement. The Lagrangian perspective follows an ensemble of particles (i.e., dye tracers, drifters and/or virtual particles) to study the evolution of the flow through a statistical approach using the trajectories. The availability of Lagrangian data to achieve these statistical analyses is more sparse relative to the availability of Eulerian data. However, a local hydrodynamic model able to reproduce observed dispersion from drifters can be useful to study the Lagrangian statistics of a system (Beron-Vera and LaCasce, 2016). Lagrangian statistics can be divided into those related to single particles and those related to multiple particles. Single particle statistics, or absolute dispersion (A^2), is obtained by estimating the mean square particle displacement from its starting position (Babiano et al., 1987; Choi et al., 2017). Multiple particle statistics, or relative dispersion (R^2), is obtained by estimating the mean square distance between pairs of particles, also known as relative dispersion (Beron-Vera and LaCasce, 2016; Sansón et al., 2017). Under various conditions, the absolute dispersion gives a classical asymptotic dispersion regime (Taylor, 1921; Babiano et al., 1987). Relative dispersion has the same asymptotic behaviour as absolute dispersion at early and late times; however, the intermediate times often show dependency on the Eulerian flow. A more detailed description of the theoretical aspect in the oceanic context is given by LaCasce (2008). Haza et al. (2008), using a local model (≤1 km) in the Adriatic sea, reported power-law behaviours near to a ballistic regime (i.e. $R^2 \approx t^2$) and anisotropic dispersion associated to the presence of a coastal boundary current. Romero et al. (2013) reported the impact of a well-defined coastline encountering that headlands are more energetic and dispersive than bays and that submesoscale processes dominate that coastal dispersion. Additional to the calculation of absolute and relative dispersion, Lagrangian probability density functions (LPDFs) have been used to provide the spatial probability of water parcels being advected from one location to another over a given period. Mitarai et al. (2009) quantified the coastal connectivity in the Southern California region using LPDFs. They stated that the dispersal patterns strongly depend on the release location, season and year, and that islands are not good sources of water parcels towards the mainland. Still, they are good receptors of water parcels from the mainland. This work demonstrated the importance of including topographic features in a local model, such as islands, when studying coastal dispersion.

1.1. Study region: The Bay of Plenty

The region of this study, the Bay of Plenty (BoP) (Fig. 1), is a large coastal embayment located on the northeast coast of Aotearoa, New Zealand, with a wide entrance of ≈190 km and a large surface area of 9.6×10^3 km^2 (Ridgway and Greig, 1986). The continental shelf region in the bay is ≈50 km wide with water shallower than 250 m (Heath, 1985; Stevens et al., 2021). The variations in the shelf width and coastline orientation can potentially lead to a system with complex physical dynamics. Offshore of the BoP, a southeastward-flowing current of subtropical water, the East Auckland Current (EAUC), carries higher temperature and salinity waters through the offshore region of the BoP (Ridgway and Greig, 1986). The EAUC is an extension of the Western Boundary Current in the South Pacific that dominates the large-scale circulation in the northeast region of Aotearoa, New Zealand. The EAUC flows along the coast from the North Cape, the northernmost point of Aotearoa, New Zealand, towards the Bay of Plenty (Heath, 1985; Stanton et al., 1997; Roemmich and Sutton, 1998; Ridgway and Dunn, 2003). At the south boundary of the EAUC, there is a quasi-stationary warm core eddy, the East Cape Eddy (ECE), that shows high variability in shape, size, and strength (Roemmich and Sutton, 1998; Tilburg et al., 2001).

Coastal circulation in the BoP is relevant as it is a pioneer in the offshore green-lipped mussel farm industry. Therefore, understanding the baseline state of the BoP is key to ensuring the sustainability of the industry and the environment. In contrast with the well-studied large-scale features in the northeast region of Aotearoa, New Zealand, scarce studies of the near-shore circulation dynamics have been made. Observationally, a 3-month study during spring 2003 found that the mean and the fluctuations of the non-tidal residual circulation were highly responsive to wind events (Longdill et al., 2008). This suggests an Ekman upwelling-driven circulation for the central area of the bay,

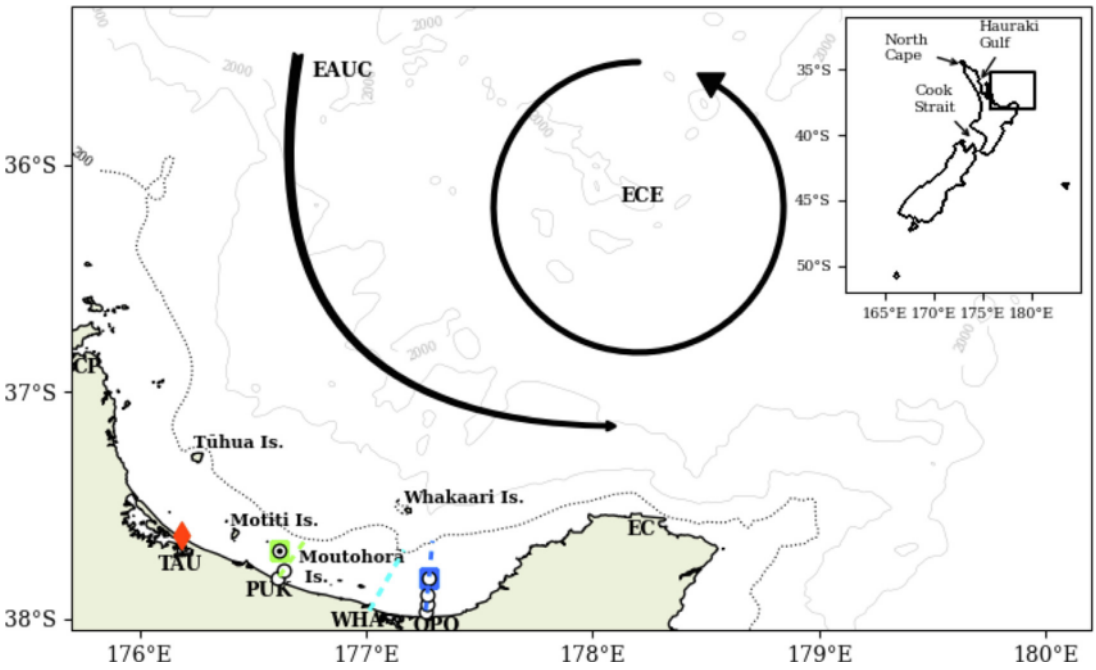

Fig. 1. Bay of Plenty model domain. Indicating regions of interest and observations used for model-data comparison and the bathymetry contours for 200 (·····), 1000 and 2000 m (——). Locations referred to in the manuscript: Tauranga (TAU,), Pukehina (PUK,), Whakatāne (WHA,), Ōpōtiki (OPO,), Coromandel Peninsula (CP) and the East Cape (EC). Symbols are observation type, which are: Wave Buoy data (•), Temperature Strings (○), Acoustic Doppler Profiler (ADP, ■), Tide Gauge ( ), Conductivity Temperature Depth transects (CTD, – – ·). The arrows ( ) are the schematic representation of the EAUC and ECE. The BoPM domain location and Aotearoa New Zealand locations mentioned throughout this study are indicated in the reference Aotearoa New Zealand map.

which is also present in other northeastern regions of Aotearoa, New Zealand (Sharples and Greig, 1998; Zeldis et al., 2004). Wind-driven currents within the BoP can reach up to 0.25 m s^{-1}, while the tidal currents on the shelf are relatively weak (0.05–0.10 m s^{-1}) (Black et al., 2005; Longdill et al., 2008).

From the modelling perspective, two-month long and one multi-year local models have been developed for the BoP in previous years. Longdill (2008) aimed to determine the potential for sustainable aquaculture within the region using a three-dimensional numerical model for a 3-month period and a 3 km horizontal resolution with 10 vertical layers up to 1000 m depth on a 207 × 114 km area. Using realistic wind forcing and boundary conditions from a free surface global circulation model (≈30 km horizontal resolution), they could replicate the wind-driven circulation and suggested that the influence of the EAUC within the BoP shelf is weak during this 3-month period. Jones et al. (2016) ran a Delft3D simulation with a 200 m horizontal resolution for a 1-month period that extended 60 km along the shore and 25 km offshore around the central BoP, aiming to forecast the dispersion of the oil spill. They stated that near-shore processes such as wind, tides and seabed roughness affected the course of particle transport. Silva et al. (2019) ran a ROMS simulation incorporating the Hauraki Gulf and the BoP to estimate current-driven larvae dispersal during November 2010–2013. This study combined population genetics with hydrodynamic modelling and found evidence of substantial interannual variability. Even though these previous studies have successfully described the wind-driven coastal circulation on an event time scale and on the central region of the BoP, the relative role of larger-scale forcing and interaction between regions has not been extensively evaluated. Having these concepts in mind, a 28-year realistic hindcast was developed for the BoP using the Moana Ocean Hindcast as boundary conditions. The aim is to establish a baseline of the Bay of Plenty with response over different time scales, from sporadic events to decadal trends.

In this study, we first describe the configuration of the 28-year coastal model and evaluate the simulation against 2 years of observations (Section 2.1). Observations, data processing and model evaluation skill metrics are described in Section 2.2. We present model evaluation results (Section 3.1) and mean circulation patterns over the coastal region of the BoP (Section 3.2). Lagrangian pathways are presented to contrast patterns under moderate upwelling favourable winds and variable wind forcing (Section 3.3). Comparisons to previous studies (Section 4.1) and Lagrangian statistics are discussed (Section 4.2), prior to a summary (Section 5).

2. Methodology

2.1. Bay of Plenty model configuration

The model implemented in this study is the Regional Ocean Modelling System (ROMS, www.myroms.org). ROMS is a primitive-equation, free-surface, terrain-following ocean model that uses the hydrostatic and Boussinesq approximations (Shchepetkin and McWilliams, 2003, 2005). The Bay of Plenty Model domain (BoPM hereinafter) is located on the northeast coast of New Zealand and covers the coastal and offshore regions of the Bay of Plenty (Fig. 1). The objective of this model is to simulate both the offshore boundary current variability and the coastal processes within the bay. The minimum depth resolved is 10 m, and the maximum depth is ≈5000 m in the basin offshore. The model grid is limited by the Coromandel Peninsula (CP) in the northwest boundary and the East Cape (EC) in the southeast, extending from 175.70 to 180.25°E and 38.06 to 35.27°S, composed of 315 × 400 grid cells with ≈1 km^2 horizontal resolution. Four islands with spatial scales larger than 1 km, Tūhua, Motiti, Moutohorā and Whakaari islands, are included as a land mask (Fig. 1).

The bathymetry for the BoPM is a merged product of GEBCO relief with a National Institute of Water and Atmospheric Research (NIWA) 250 m resolution bathymetry dataset for New Zealand coastal waters (Mitchell et al., 2012). The NIWA dataset is bin-averaged and sampled at 1 km to match the target BoPM grid horizontal resolution. In ROMS, two grid metrics are used to quantify and limit numerical errors due to steep sea-bed slopes, the so-called Beckman and Haidvogel number (rx_0) and a hydrostatic inconsistency number (rx_1) (Beckmann and Haidvogel, 1993; Haney, 1991). The first number

is the topographic stiffness ratio, and the latter introduces the limitation for the slope of stretched terrain-following coordinates (σ-coordinates) between two adjacent wet points. A linear programming procedure is used to smooth the bathymetry, preserving volume while avoiding significant modifications to the bathymetry (Sikirić et al., 2009). The rx_0 and rx_1 numbers were reduced to maximum values of 0.08 and 4.75, respectively. Idealised tests of 5-day simulations with closed boundaries, no external forcing, and initialised with a horizontally-uniform temperature profile were performed to optimise the vertical coordinate parameter configuration and maintain minimal numerical error. The final configuration is similar to that of the Moana Ocean Hindcast. It consists of 50 vertical layers using a quadratic Legendre polynomial vertical stretching function with an emphasis on resolving the surface layer (Souza et al., 2015). Grid stretching factors of 2 are used for the bottom (θ_b) and 6 for the surface (θ_s), with a boundary layer thickness parameter of 100 (T_{cline}).

The technique of one-way nesting is used such that an independent coarse resolution model (parent simulation) provides boundary conditions interpolated in time and space to a higher-resolution model (child simulation) (Mason et al., 2010). The 28-year Moana Ocean Hindcast with 5 km horizontal resolution and realistic atmospheric, tidal and regional boundary forcing serves as the parent simulation (Fig. 1 inset). Radiative boundary conditions are combined with a ≈40 km nudging region adjacent to the four open boundaries of BoPM simulation. Nudging of temperature and salinity towards the daily averaged Moana Ocean Hindcast is stronger near the boundaries (0.5 day^{-1}) and linearly decreases towards the domain interior (0.01 day^{-1}). Implicit Chapman and Flather boundary conditions were used for the free surface and the barotropic velocities, respectively (Solano et al., 2020).

The BoPM is driven at the surface with the "Climate Forecast System Reanalysis" (CFSR) atmospheric fields (Dee et al., 2014). The variables provided by CFSR are sea level pressure, 10 m winds, air temperature, relative humidity, precipitation rate, long wave and downward short radiation, the same forcing as the Moana Ocean Hindcast. ROMS internally calculates air–sea heat and momentum fluxes from the CFSR atmospheric fields, with an adaptation of the parametrisation described by Fairall et al. (1996a,b). The inverse barometer effect, essential to producing accurate large-scale sea surface height and ocean circulation response around New Zealand, is also used in this configuration (Souza et al., 2022). When using nested models, the amplitudes of the tides can be significantly reduced if the tidal spectral forcing is not specified separately (Janeković and Powell, 2012). Therefore, the tidal signal is extracted from the barotropic fields of the boundary conditions obtained from the Moana Ocean Hindcast and introduced to the BoPM as barotropic spectral forcing.

2.2. Model evaluation

2.2.1. Bay of Plenty observations

The skill of the BoPM was assessed using a variety of measurements of oceanic variables, such as temperature, salinity, sea surface height and velocity components for the 2003–04 period over the Bay of Plenty (Table 1, Fig. 1). This period was chosen due to the number of available observational datasets with a range of spatial and temporal coverage, including continuous time series and seasonal measurements at different depths and locations along the coast. These datasets include hourly time series of meteorological, velocity, temperature data, and CTD profiles collected by Longdill (2008) and Longdill et al. (2008). The atmospheric forcing was evaluated due to the known influence of local winds on the coastal circulation. Each set of observations was subjected to a processing procedure according to the type of measurement (profile, single point and time-frequency of the data). To evaluate the BoPM output, the respective data sets were extracted using interpolation from the daily or hourly model output. If the location was within a masked point on the grid, the nearest grid wet point was selected instead of extrapolating. Afterwards, the interpolated model output was subjected to the same processing as the observations.

The wind speed, wind direction, and mean sea level pressure (MSLP) from CFSR were compared to the Tauranga airport hourly meteorological measurements to evaluate the atmospheric forcing. The wind stress was calculated using the bulk formula $\vec{\tau} = C_d \rho_a V \vec{V}$, where C_d is a drag coefficient obtained using Coupled Ocean–Atmosphere Response Experiment (COARE) 3.5 algorithms (Edson et al., 2013; Ludovic et al., 2021), ρ_a is the air density, and V is the wind speed at 10 m above the sea surface. A Principal Component Analysis (PCA) was applied to obtain the along-shore and cross-shore wind stress components (orientation of 108 ± 5°). Temporal variability shorter than 40 h was filtered using a low band-pass filter (State Estimation and Analysis in PYthon (SEAPY) package).

Hourly sea surface height data from the tide gauge located on Moturiki Island for the 2003–2004 period was compared with the BoPM output to assess the tidal and non-tidal sea level variability. The tidal analysis was done using the T_Tide Python package (Pawlowicz et al., 2002). The three major tidal constituents M_2, N_2 and S_2 were reported. The M_2 tidal constituent has the largest amplitude (≈0.7 m), followed by N_2 and S_2 (≈0.1 m).

The tidal and non-tidal velocity was evaluated using velocity data from two different locations at the 65-m isobath obtained by a single SONTEK 500 kHz Acoustic Doppler Profiler (ADP) as an hourly-averaged output from 5-min period measurements, of 2-m bins, along the first 60 m of the water column. For this analysis, the first 3 bins (6 m) of the near-surface water column were removed. For the tidal components, a harmonic analysis was done using the velocity time series as a complex vector $vel = u + iv$ to obtain the tidal ellipse with the T_Tide Python package (Pawlowicz et al., 2002). The values for the major axis and the minor axes of the tidal ellipse are reported for the three main tidal constituents M_2, N_2 and S_2. A PCA was applied to obtain the along-shore and cross-shore velocity components of the non-tidal velocity. The new orientation for the major axis in the along-shore cross-shore coordinate system is of 124±5°, 119±5°, 100±5° for western (TAU), central (PUK) and eastern (OPO) BoP, respectively (for location reference see map in Fig. 1). To analyse the vertical structure, the standard deviation for each 2 m depth bin was calculated from the rotated velocity data.

To evaluate the temperature at different shallow depths and through time, a total of 25 time series from Remotely sensed SST, thermistor arrays and a wave buoy were compared with the BoPM output. Remotely sensed SST was obtained from version 4.1 of the Multiscale Ultrahigh Resolution (MUR) Level 4 analysis from Group for High-Resolution Sea Surface Temperature (GHRSST) (MUR GHRSST). This product delivers global daily SST on a 0.1° grid resolution. It is a fusion of SST observations from several instruments such as microwave radiometers, satellites and in situ observations (Chin et al., 2017). In this study, MUR GHRSST was separated between nearshore (MUR Nearshore) and offshore (MUR Offshore), delimited by the 200 m isobath. The spatial mean of these areas was done to obtain a 2-year time series of the SST of the nearshore and offshore area. The thermistor arrays were obtained using StowAway TidbiT sensors in seven different locations within two regions at various depths (1, 2, 5, 8, 10, 15, 20, 30 m) depending the location (Fig. 1, Table 1). The last sea surface temperature time series is provided by the Bay of Plenty Regional Council (BoPRC). This is part of a wave buoy located 13 km offshore from the Pukehina beach around the 65 m isobath (BoPRC Data link). The thermistor arrays and wave buoy provided hourly temperature data averaged daily for comparison purposes.

Finally, vertical profiles of salinity and temperature were assessed using CTD data collected by Longdill (2008). The vertical profiles of temperature and conductivity (salinity) were measured by a SEABIRD SBE 19+ Seacat Profiler along three transects (Ōpōtiki, Pukehina and Whakatāne) with 6 profiles each, the most shallow profile being on the 10 m isobath and the deepest on the 200 m isobath. These surveys were

Table 1
Observations collected from the BoP region during 2003–2004. The regions of data collection: Tauranga (TAU), Pukehina (PUK), Whakatāne (WHA), Ōpōtiki (OPO), and Bay of Plenty (BoP).

ID	Depth coverage	Temporal coverage	No. of observations	Region	Longitude	Latitude
Atmospheric data time series						
Wind	Surface	01/01/03–09/12/04	16 993	TAU	176.196	−37.673
MSLP	Surface	01/01/03–09/12/04	16 993	TAU	176.196	−37.673
Sea surface height time series						
TG	Surface	01/01/03–31/12/04	17 540	TAU	176.183	−37.633
Velocity components time series						
ADP OPO	10–60m	12/06/04–22/10/04	3002 × 26	OPO	177.278	−37.818
ADP PUK	10–60 m	24/09/03–01/12/03	1604 × 26	PUK	176.616	−37.696
Temperature time series						
MUR	Surface	01/01/03–31/12/07	431 × 291 × 1826	BoP	Grid domain	
WB	Surface	01/10/03–31/12/04	467	PUK	176.616	−37.696
OPO15	1, 5, 10, 15 m	19/03/04–06/12/04	263, 182, 46, 182		177.263	−37.968
OPO30	1, 5, 10 m	22/10/04–06/12/04	46, 46, 46	OPO	177.266	−37.935
OPO40	1, 5, 10 m	22/10/04–06/12/04	46, 46, 46		177.270	−37.898
OPO65	2, 8, 20 m	07/06/04–22/10/04	127, 127, 127		176.278	−37.818
PUK15	1, 5, 15 m	04/12/03–19/03/04	110, 110, 110		176.611	−37.822
PUK30	1, 5, 10, 30 m	04/12/03–19/03/04	107, 107, 107, 107	PUK	176.636	−37.787
PUK65	2, 8, 20 m	17/09/03–19/03/04	183, 183, 183		176.616	−37.696
Temperature and salinity profiles						
CTD OPO	0–10 m, 0–20 m,	Summer		OPO	177.263	−37.964
	0–30 m, 0–50 m,	(03/12/03, 28/03/04)	140		⋮	⋮
	0–100 m, 0–200 m	Winter			177.294	−37.658
		(17/10/03, 01/08/04)	140			
CTD PUK	0–10 m, 0–20 m,	Summer		PUK	176.617	−37.814
	0–30 m, 0–50 m,	(03/12/03, 28/03/04)	154		⋮	⋮
	0–100 m, 0–200 m	Winter			176.740	−37.642
		(17/10/03, 01/08/04)	148			
CTD WHA	0–10 m, 0–20 m,	Summer		WHA	177.015	−37.934
	0–30 m, 0–50 m,	(03/12/03, 28/03/04)	148		⋮	⋮
	0–100 m, 0–200 m	Winter			177.167	−37.698
		(17/10/03, 01/08/04)	151			

done on four dates; for the seasonality aspect, these were separated between Summer and Winter. Summer being the deployments done during December and March, and Winter being the ones deployed during August and October. To maintain two cohorts of data, the survey made during mid-spring (17/10/03) is considered a winter deployment, given that the surface and mid-water salinity and temperature values were consistent with the ones measured during winter. This data was used to analyse the vertical structure of the water column. Due to the data set not having an hourly time stamp, the comparison was made using the daily average of the BoPM. The water column was divided into 5 m depth bins to reduce the noise. For comparison purposes, the 60+ CTD casts were also separated into clusters characterised by the depth of the water column in which the deployment was done. Regarding the depth, the data was separated between shallow and deep. Shallow being for the profiles deployed within the 50 m isobath limit (10, 20, 50 m isobath) and deep profiles being the ones deployed at the 100 and 200 m isobaths.

2.2.2. Skill metrics

The evaluation of the BoPM is done using three metrics: the mean bias (MB, Eq. (1)), the Root Mean Square Error (RMS, Eq. (2)) and the Willmott skill score (D, Eq. (3)) (Willmott, 1981). A combination of these metrics has been commonly used to assess the model skill to reproduce the observations and quantify the error on a variety of regions such as estuaries (Warner et al., 2005; Kärnä et al., 2015; Liu et al., 2009), and high-resolution coastal models (Wilkin, 2006; Zhang et al., 2019). The MB and the RMS are metrics that show the difference between the observations and the model and the standard deviation of the residuals, respectively. These metrics have the same units as the analysed variable. The Willmott skill score is a non-dimensional quantitative metric in the range of 0 to 1 as a measure of the agreement between the observed and modelled data. The highest value (1) denotes perfect agreement between the model and the observations. These metrics are defined as:

$$MB = \langle M_i - O_i \rangle \tag{1}$$

$$RMS = \sqrt{\langle (O_i - M_i)^2 \rangle} \tag{2}$$

$$D = 1 - \frac{\langle (O_i - M_i)^2 \rangle}{\left\langle \left[|M_i - \langle O \rangle| + |O_i - \langle O \rangle| \right]^2 \right\rangle} \tag{3}$$

where $\langle\ \rangle$ denotes the average over the series, letting O_i and M_i, $i = 1 \ldots N$, be the observation and the associated model result respectively.

In addition to these metrics, Taylor and Target diagrams were used. Taylor and Target diagrams provide a concise statistical summary of how well patterns match each other in terms of their correlation, Bias, RMS and the ratio of their variances (Taylor, 2001). The Taylor diagram used in this study shows the correlation coefficient between the observations and modelled data and the normalised standard deviation σ_{m_NORM}. The standard deviation was normalised using the standard deviation of the observation $\sigma_{m\_NORM} = \sigma_m/\sigma_o$, this allows to identify if the variance of the observations is well represented. The Target diagram complements the information shown in the Taylor diagram by showing the RMS and the Bias.

3. Results

3.1. Model evaluation

We first compare CFSR atmospheric variables, along- and cross-shore wind stress and MSLP, to observations from the Tauranga airport and Tauranga tide gauge (Fig. 2). The model skill for these variables was 0.80 and 0.73 with RMS values of 0.29 and 0.23 N m^{-2} for the along- and cross-shore wind stress, respectively and a model skill of 0.97 and RMS value of 3.04 mb for the MSLP. These values confirm that CFSR atmospheric forcings have a realistic representation of the observed variability on coastal scales. Due to the coastline orientation of the BoP on Tauranga, winds with significant NW and SE components can induce upwelling and downwelling circulation patterns over the

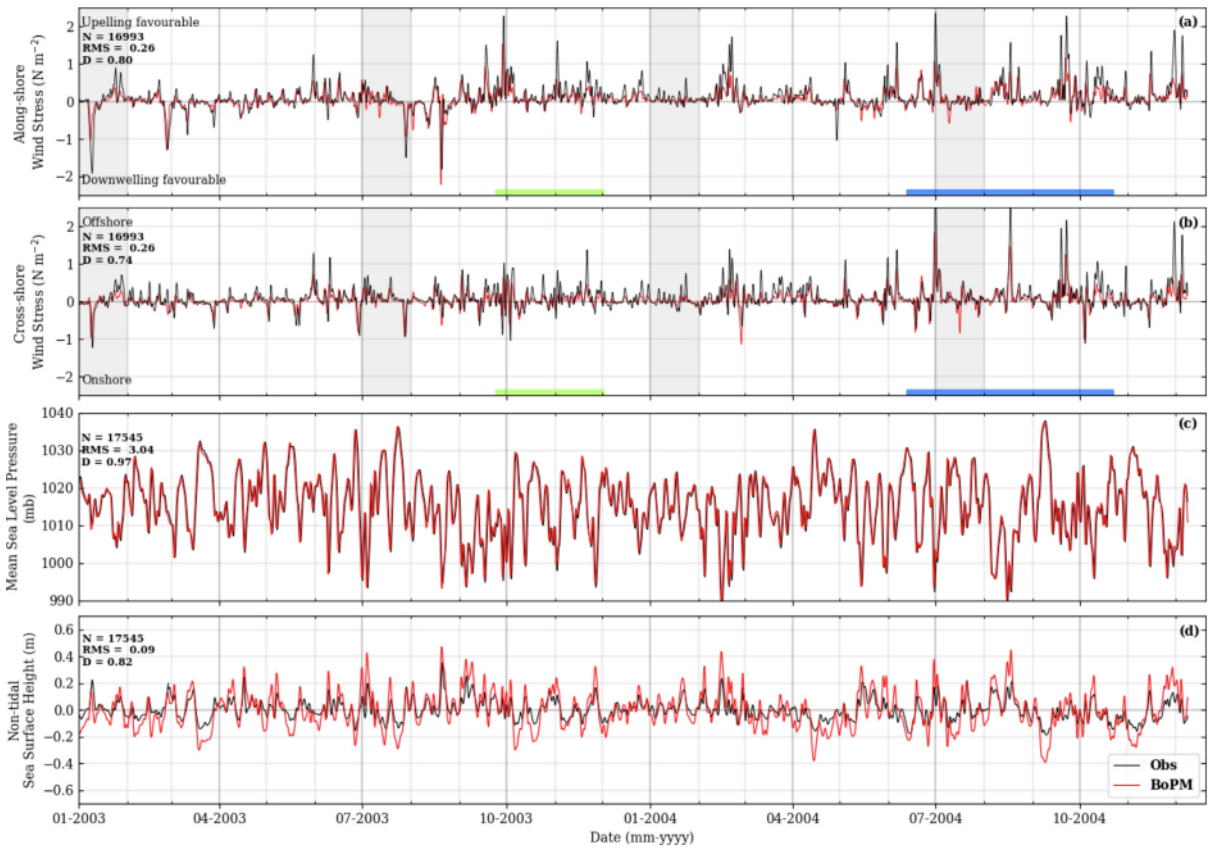

Fig. 2. Comparison of observed (——) and model (——) Hourly-low pass-filtered meteorological variables. (a–b) Along-shore (a) and cross-shore (b) wind stress (N m^{-2}). (c) Mean Sea Level Pressure (mb). (d) Comparison of hourly time series of observed and simulated low pass-filtered non-tidal Sea Surface Level (m, bottom panel). The colours in the top panels indicate the periods of ADP observations for Pukehina ( ) and Ōpōtiki ( ). The grey-shaded panels highlight the January and July months, which are relevant further in the study. The number of observations (N) and the values of RMS and D, as defined in Eqs. (2) and (3), are present in each panel. (For interpretation of the references to colour in this figure legend, the reader is referred to the web version of this article.)

shelf. During January, the wind stress is relatively weak, and the along-shore component has a persistent direction towards SE for the most part, except for an intense event towards the NW at the beginning of 2003. During July, the wind stress is more variable in both components and more intense relative to January, especially during 2004. For the non-tidal sea level, the results show that the model can reproduce the seasonal and inter-annual variability with a skill score of 0.82 and a RMS of 0.09 m. Both the observations and the simulated data have a relatively low positive correlation ($p < 0.05$) with the wind stress (≈0.25) and a high inverse correlation ($p < 0.05$) with the MSLP (≈−0.75). Thus demonstrating that the model and observed non-tidal sea level response are strongly dominated by the inverse barometer effect across event-scale to seasonal time scales.

The sea surface height and velocities were used to evaluate the tidal component of the simulation (Table 2). The results show that the sea level in Tauranga the BoPM has a −7 cm difference for the M_2 constituent and a <1 cm difference for the other two constituents (N_2, S_2), which is about an order of magnitude smaller than the amplitude of the constituents. There is a difference in the phase of ≈0.6 h amongst the constituents. The differences between the observations and the simulation might be due to the proximity of the tide gauge to the Tauranga estuary mouth, which is not represented in the BoPM. If the tidal spectral forcing is not specified separately, as mentioned in Section 2.1, the BoPM performs worse. The harmonic method, suggested by Janeković and Powell (2012), improved the values of the simulated amplitude by ≈13 cm for the M_2 constituent and ≈5 cm for the N_2, S_2 constituents (not shown). Moreover, the major axis of tidal velocity compares well between BoPM and observations (Table 2). There is a larger difference in PUK of 0.52 cm s^{-1} in contrast with OPO of 0.04 cm s^{-1} for the M_2 constituent. Meanwhile for N_2 (S_2) the difference is of 0.01 (0.01) cm s^{-1} for OPO and of 0.06 (0.27) cm s^{-1} for PUK. The minor axis has a larger difference for OPO compared to PUK, with a value of −1.35 and −0.36 cm s^{-1} respectively for the M_2 constituent. It shows that the BoPM has more variability in the minor axis than the observations over the OPO region. In the case of the phase, the differences at the OPO and PUK locations for the M_2 tidal constituent are 5.1° and 8.7°, respectively. This value is relatively smaller than the 23° difference seen for the TG. The phase differences of the N_2 (S_2) constituents are relatively smaller at these locations compared with the TG values of 34.7° (23.1°) difference and with values of 18.3° (10.1°) at OPO and 17.9° (10.3°) at PUK. Overall, these results show that the

Table 2
Evaluation results of the M_2, N_2 and S_2 tidal constituents at the Tide Gauge (TG) in Motouriki and the two ADP locations Ōpōtiki and Pukehina.

	M_2		N_2		S_2	
	Obs	BoPM	Obs	BoPM	Obs	BoPM
Amplitude m)						
TG	0.72	0.65	0.15	0.14	0.10	0.09
Major axis cm s^{-1})						
ADP OPO	3.23	3.27	0.68	0.67	0.43	0.42
ADP PUK	2.63	2.11	0.65	0.38	0.39	0.25
Minor axis cm s^{-1})						
ADP OPO	0.29	1.64	0.03	0.53	0.22	0.03
ADP PUK	0.75	1.11	0.08	0.14	0.39	0.07
Phase °)						
TG	175.4	198.4	140.3	175.0	250.9	274.8
ADP OPO	271.7	276.8	224.9	243.2	357.3	7.4
ADP PUK	274.3	283.0	241.0	258.9	314.8	325.1

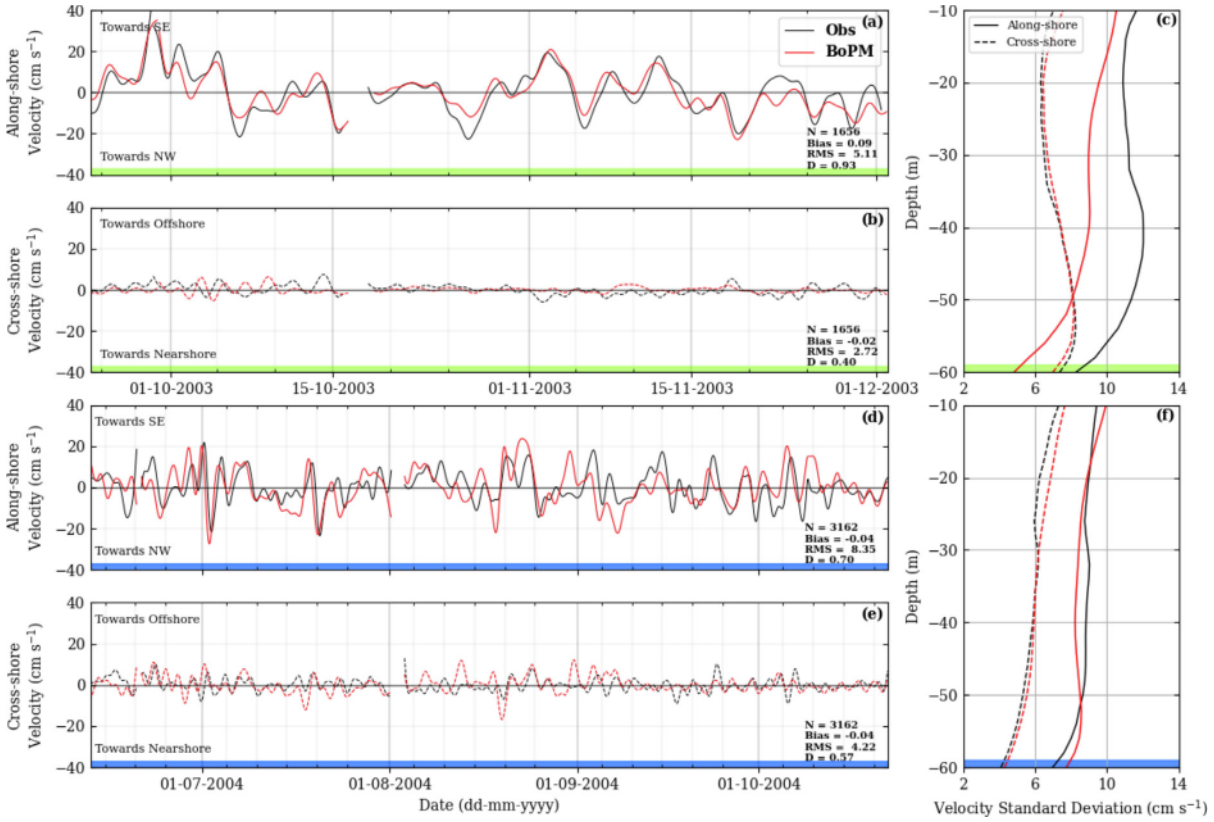

Fig. 3. (a, b, d, e) Comparison of the time series of the low-passed filtered observed (——) and model derived (——) depth-averaged along-shore and cross-shore velocity components (cm s^{-1}) for the two ADP locations. Pukehina ( ) sampling period between 24/Sept/2003 and 01/Dec/2003 and Ōpōtiki ( ) sampling period between 12/Jun/2004 and 22/Oct/2004. (c, f) Vertical profile of the standard deviation calculated from detided hourly time series in 2 m depth bins of the along-shore (—) and cross-shore (- - -) velocity components for the two ADP locations Pukehina ( ) and Ōpōtiki ( ). The number of observations (N) and the values of mean bias, RMS and D, as defined in Eqs. (1), (2) and (3), are present in each panel (a,b,d,e).

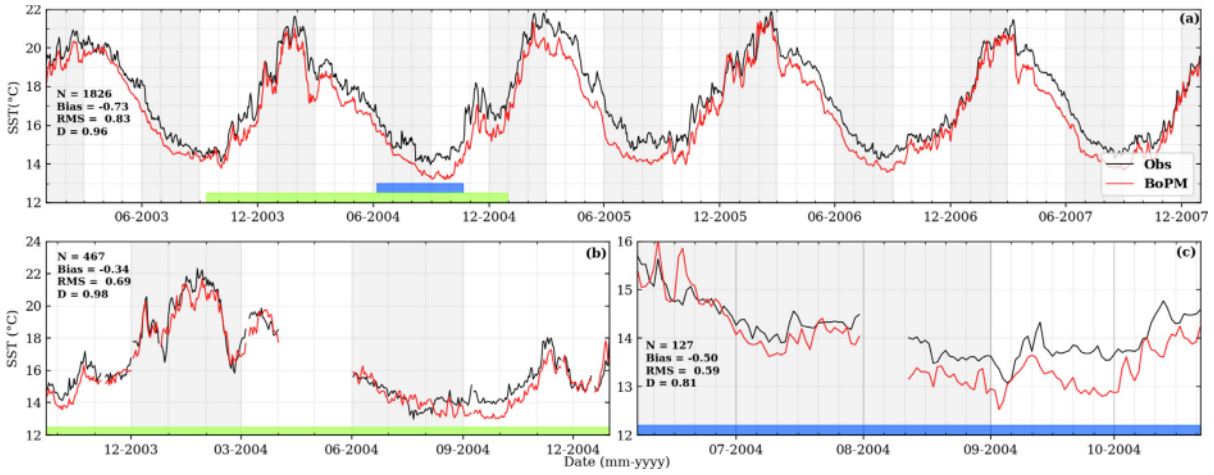

Fig. 4. Comparison between model derived (——) and observed (——) sea surface temperature at different locations and periods. (a) Satellite-derived daily averaged SST data compared to model daily averaged SST output time series spatially averaged to represent the nearshore area (MUR) of the BoP between 2003–2007. (b) Daily averaged SST thermistor data compared to model daily averaged SST output at Pukehina (WB,) between 22/Sept/2003 and 31/Dec/2004. (c) Daily averaged SST thermistor data compared to model daily-averaged SST output at Ōpōtiki (OPO65,) between 07/Jun/2004 and 22/Oct/2004.

phase, amplitude and tidal velocities in the semi-diurnal tidal band are well represented in the BoPM.

The filtered time series of the rotated depth-averaged along-shore velocity at two different locations shows a good representation of the variability. The model has a better reproduction of the variability at the PUK location with a skill score of 0.93 compared to the 0.70 value at OPO (Fig. 3). Note, the OPO location was observed in winter, where model-data differences are more significant (Figs. 4, 5). The filtered depth-averaged cross-shore velocities are smaller in magnitude, especially for PUK with velocities ≤5 cm s^{-1} for most of the period. The averaged cross-shore velocities show more discrepancy, with skill score values of 0.40 and 0.57 for PUK and OPO, respectively. The relatively low values can be associated with the magnitude of the cross-shore component. However, as seen in the along-shore component, there is a relatively good representation of the variability in both locations. It has been reported that the currents in the central BoP are very responsive to

winds (Longdill et al., 2008). An example of this is represented at the PUK location. Towards the end of September 2003, there is a strong upwelling favourable wind event (from NW, Fig. 2). At this time, both observed and modelled flows are heading towards the SE (Fig. 3(a)). The near-surface flows are heading offshore, and the near-bed flows are shoreward (not shown). These patterns are consistent with wind-driven coastal upwelling.

The structure of the vertical standard deviation of the velocity components is well represented in the model, reproducing lower values of cross-shore velocity variability in contrast with the along-shore velocity. For the PUK location, the observed along-shore velocity shows more variability through the water column compared to the model. Results show a maximum difference at 40 m depth with a standard deviation of ≈12 cm s^{-1} in the observations and of ≈9 cm s^{-1} in the simulation (Fig. 3(c)). The water column in PUK shows a stronger variability for the along-shore component and more variability through the profile. The PUK depth-average velocity shows a very dominant along-shore component and a very weak cross-shore component (Figs. 3(a)–3(b)). Meanwhile, in OPO, the water column shows less variability throughout the water column (Fig. 3(f)). The depth-average velocity shows a cross-shore component slightly stronger relative to PUK and more variability in both components (Figs. 3(d)–3(e)). This could be associated with the period when the measurements were taken. This winter period has stronger and highly variable winds relative to the PUK period (Fig. 2), which can be associated with a strongly mixed water column.

Three time series are represented in Fig. 4 showing 5 years of spatially averaged nearshore SST (MUR Nearshore), 14 months of SST at PUK (WB), and ≈4 winter months of SST at OPO. These time series were chosen to represent the temperature comparison highlighting regional and local results. Overall, the time series show a larger offset during the winter months (May–August). In the three time series, during August–October of 2004, there is a maximum offset of up to ≈1 °C. This colder offset is present as a larger bias, relative to the BoPM, in the Moana Ocean Hindcast (parent model, Fig. 6). More analyses are needed to identify if the colder offset is inherited by the choice of atmospheric forcing or due to the model configuration of mixing parameters. Meanwhile, during the summer months, there is a very good agreement between the observations and the BoPM.

The statistics for all the temperature time series are represented in a Taylor Diagram (Fig. 6(a)) (Taylor, 2001). The Taylor diagram shows the normalised standard deviation and the correlation coefficient. The BoPM shows a reliable capability of reproducing the sea surface and subsurface (20–30 m depth) temperature observations, presenting a high correlation above 0.8 for all the time series (Fig. 6(a)). In the OPO region, the variability is slightly underestimated for most of the nearshore measurements, except for the 10 m and 15 m depth time series of the OPO15 station, where the values are closer to the unit. Note, the locations OPO30 and OPO40 are the time series with fewer observations (N≈46). Meanwhile, most offshore OPO measurement variability is overestimated. The PUK region is generally closer to the unit and does not show any significant differences between the depth of the measurements. The time series longer than one year (WB, MUR Offshore and MUR Nearshore) show a well-represented variability with values of normalised standard deviation close to 1 and a correlation coefficient above 0.95.

The comparison of the 60+ CTD casts temperature shows a colder bias tendency and a smaller error during summer months for the BoPM (• and ■ in Fig. 5(a)). There is a higher negative MB during winter months with a value of −0.40 °C and a RMS of 0.59 °C for the shallow profiles (○), and a MB of −0.60 °C and a RMS of 0.88 °C for the deep profiles (□). Meanwhile, during summer, the data presents a smaller cold bias of −0.15 °C and a RMS of 0.55 °C for the shallow (•) and a bias of −0.27 °C with a RMS off 0.68 °C for the deep profiles (■). The salinity evaluation for the summer period presents RMS values of 0.13 for the shallow profiles (•) and 0.08 for the deep profiles (■). During winter, the results show a larger discrepancy, the shallow profiles (○) present a bias of 0.39 and a RMS value of 0.70, and a bias of −0.01 and a RMS value of 0.22 for the deeper profiles (□). During mid-July 2004, there was an exceptional flooding event throughout the Bay of Plenty (NIWA, 2022). Longdill (2008) noticed an inverse thermal profile in the area during this period due to the flooding events. Ignoring CTD casts during this period (1-Aug-2004) removes outliers and improves the RMS from 0.7 to 0.6. These results and previous studies (i.e. Longdill, 2008) suggest that further improvements are needed to model the river influence accurately (i.e. model parametrisation, accurate flux data, higher spatial resolution). The BoPM has a better ability to reproduce observed salinity during the summer period relative to the winter period. On the large scale, the BoPM reproduces the spatial distribution of salinity throughout the domain that increases with distance offshore. On the coastal scale, there is a lack of river influence, which is reflected in the coastal areas (around the 10 and 20 m isobath) in locations near river mouths during the winter period.

The impact of increasing the resolution and the addition of a more defined coastline and islands was assessed in comparison to the Moana Ocean Hindcast (Souza, 2022). The summary of the temperature time series comparison is displayed using a Target diagram (Figs. 6(b)–6(c)). The Target diagrams complement the Taylor diagram information by showing the data sets' RMS and MB. The BoPM shows an improvement over the Moana Ocean Hindcast of at least 0.5 °C in the RMS and the MB (Figs. 6(b), 6(c)). There is an average difference of 0.8 °C between the BoPM and the Moana Ocean Hindcast. The MUR Offshore data showed a more significant improvement in BoPM with an RMS value of 0.5 °C compared to the 1.9 °C for Moana Ocean Hindcast. This suggests that the BoPM not only enhances the coastal region, but it also improves model performance offshore.

The BoPM presents an improvement over the Moana Ocean Hindcast in simulating water column temperature and velocity and a similar performance in simulating water column salinity. The Moana Hindcast reported a higher offset during winter for the temperature and the cross-shore velocity component. The cross-shore component showed an increase of the model skill from 0.49 to 0.57, and the water column temperature showed a RMS decrease from ≈1.3 °C to ≈0.6 °C. The water column salinity of the Moana Ocean Hindcast also showed an offset, likely because of the lack of representation of extreme flooding events. During summer, the Moana Ocean Hindcast has a RMS value of 0.15 on the shallow profiles and 0.14 on the deep profiles showing that the BoPM has a slight improvement of 0.02 and 0.06 on the shallow and deep profiles, respectively. During winter Moana Ocean Hindcast has a RMS value of 0.69 and 0.22 for the shallow and deep profiles, respectively, similar to the 0.70 and 0.22 values obtained from the BoPM. The tidal evaluation presents similar values between the Moana Ocean Hindcast and the BoPM, with the difference between the observed and modelled values of the M_2 N_2 and S_2 tidal constituents for both simulations being less than 10 of the observed amplitude. For more information regarding the evaluation of the Moana Ocean Hindcast, refer to Souza et al. (2022). The outperformance of the BoPM over the Moana Ocean Hindcast is consistent with previous modelling studies that suggest that increasing the resolution can lead to improving the skill of a model by taking into account submesoscale processes (e.g., Haza et al., 2008), the impact of islands (e.g., Dong and McWilliams, 2007), and/or having a better resolved bay-shelf exchange (e.g., Zhang et al., 2019).

3.2. Circulation patterns and wind-driven flow

Throughout the year, the BoP shows differences in the large-scale circulation, atmospheric forcing and coastal flow variability. In this section, we contrast model average circulation and temperature anomaly between January and July 2003–2004. The mean sea surface temperature during January is 20.3 °C, which is 4.7 °C higher than the average 15.6 °C reported during July conditions (Figs. 7(a), 7(b)). Both months present a band of cold water anomaly near the shore

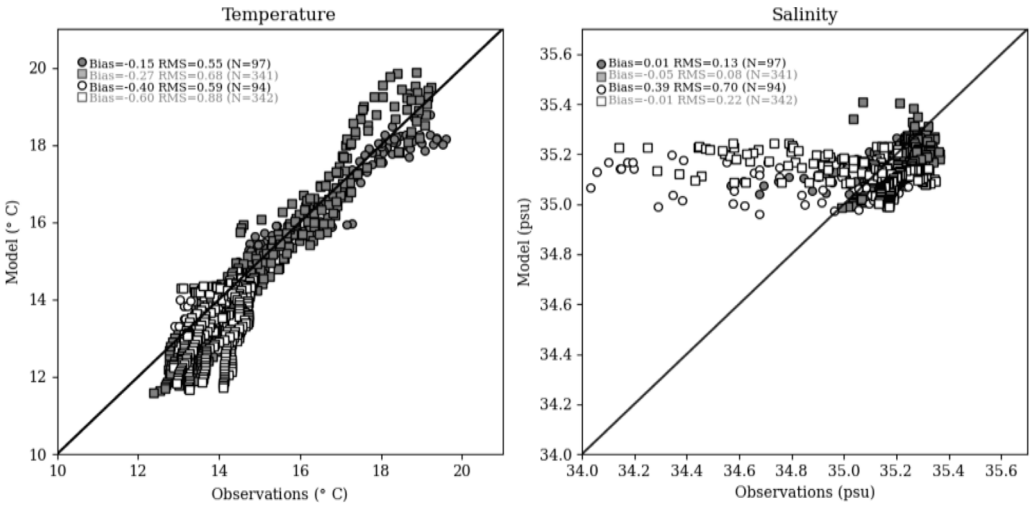

Fig. 5. Scatter plot between the in situ CTD data and the BoPM output. Temperature (a) and Salinity (b), at different depths and locations (For more details, see Table 1). The markers indicate if they are shallow profiles (10, 20, 30 and 50 m isobath, ∘) or deep profiles (100–200 m isobath, ■) The colours indicate the season in which the measurement was taken, Summer (∘, ■) or Winter (∘, □). N is the number of samples, and the values of bias and RMS corresponding to the evaluation are present in each figure.

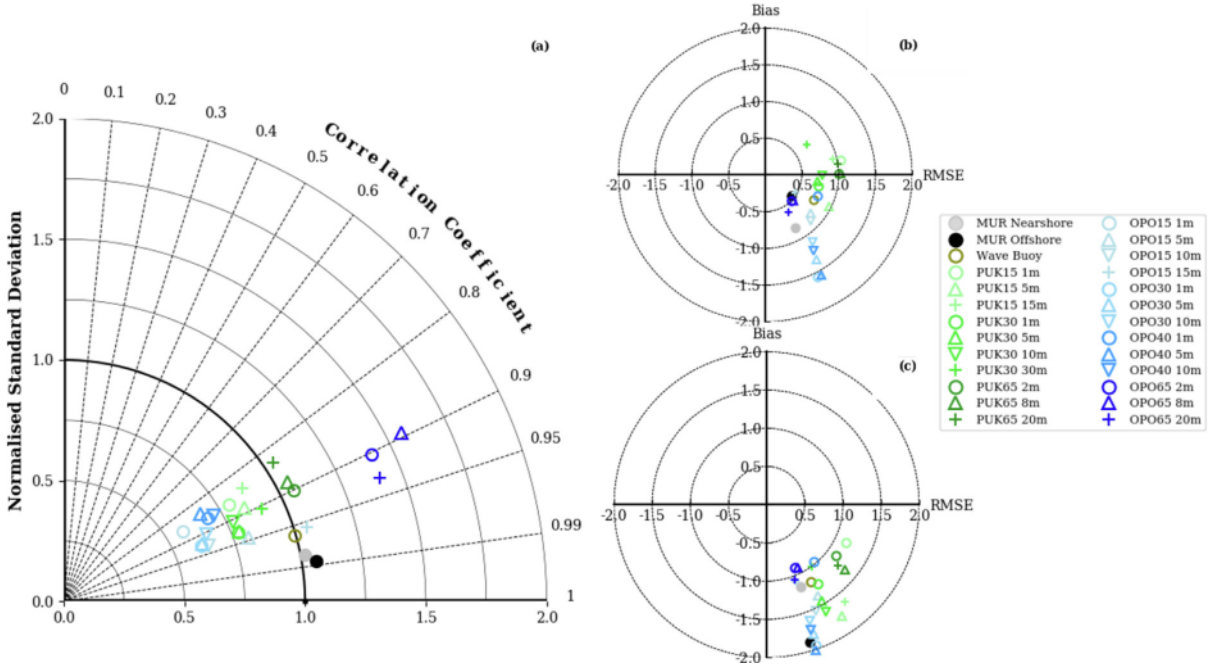

Fig. 6. Comparison of observed temperature time series used to evaluate the BoPM using a Taylor diagram. The Taylor diagram displays the correlation coefficient and the normalised standard deviation. (b–c) Comparison of observed temperature time series used to evaluate the BoPM (b) and the Moana Ocean Hindcast (c) using a Target diagram. The Target diagram displays the mean bias and the RMSE. The colours indicate one of the four regional divisions, Ōpōtiki (■), Pukehina (■), Wave Buoy (■), BoP domain (■), lighter shades represent the proximity to shore. The marker represents the depth, having observations at the surface (∘), 5–8 m (△), 10 m (▽), and below 15 m (+). For more details of the observed data, see Table 1. (For interpretation of the references to colour in this figure legend, the reader is referred to the web version of this article.)

of ≈1 °C and 2 °C for January and July, respectively, suggesting coastal upwelling. During January, the winds are primarily bidirectional, having predominantly upwelling-favourable winds followed by downwelling-favourable winds, referred to as January conditions hereinafter (Fig. 7(c)). Meanwhile, during July, the wind direction is more variable, and winds with higher speeds (>10 m s^{-1}) are more frequent, referred to as July conditions hereinafter (Fig. 7(d)). The intensification of the cold water anomaly during July conditions is due to strong wind-driven mixing that can be explained by the strong and high-variable winds, characteristic of event-scale storm systems that tend to deepen the mixed layer through wind-driven mixing.

The ECE and the EAUC, mesoscale features show variability in their strength and position between January and July conditions. This variability is observed using maps of the spatial SST anomaly, mean flow and mean streamlines (Fig. 7). The streamlines are lines of constant values of the stream function (ψ) defined by solving $u = \partial\psi/\partial y$ and $v = -\partial\psi/\partial x$, where u and v are the east–west, and north–south components of the monthly averaged modelled surface current. The SST anomaly and the mean flow map show these mesoscale features as warm anomalies, with the ECE being a warm-core anticyclonic eddy (anti-clockwise circulation) and the EAUC being a south-eastward flowing large-scale boundary current carrying subtropical waters. During January conditions, the EAUC and the ECE are closer to the shelf. The EAUC has a mean flow ≈25–30 cm s^{-1} with an intensification offshore of the East Cape reaching velocities of 40 cm s^{-1}. The mean field shows an asymmetric ECE, with the eastern side elongated relative

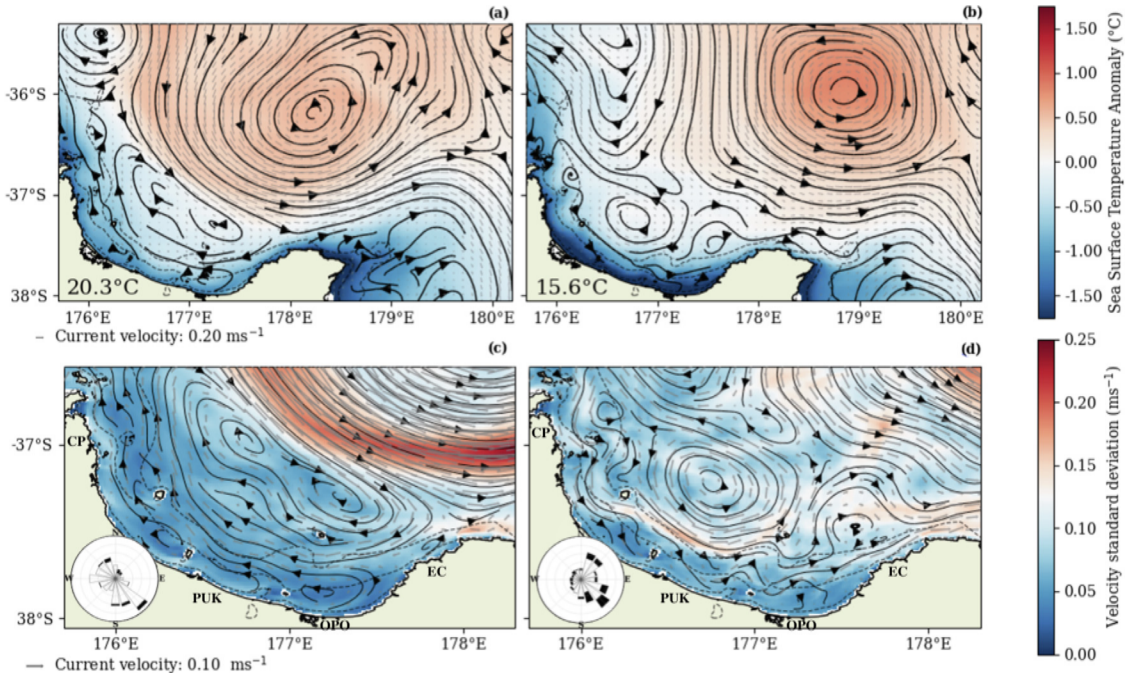

Fig. 7. (a–b) Spatial anomaly of the sea surface temperature average (°C, colour map) corresponding to January and July (2003–2004) for the BoPM domain. The number over the landmask represents the sea surface temperature spatial average (°C). (c–d) Zoom in on the BoP showing the standard deviation velocity (m s^{-1}, colour map) over the first 10 m of the water column, corresponding to January and July (2003–2004). The windrose over the landmask corresponds to a point in the central region of the bay for each given period. The colour indicates the magnitude of the wind (■ > 10 m s^{-1} and □ < 10 m s^{-1}). Mean streamlines ( ), mean currents ( ), and the 20, 65 and 200 m isobaths (– – ·) are shown in all the panels. (For interpretation of the references to colour in this figure legend, the reader is referred to the web version of this article.)

to the western side, centred at 178.2°E, 36.2°S (Fig. 7(a)). Over the shelf, delimited by the 200 m isobath, the flow has less variability relative to July conditions and shows a more organised westward flow. During July conditions, the EAUC and the ECE are located further away from the shelf. The EAUC has a mean flow of ≈15–20 cm s^{-1}, and the maximum values of velocities are associated with the ECE with ≈34 cm s^{-1}. The mean field shows that the ECE centre lies at 178.9°E, 36.0°S (Fig. 7(b)). As a consequence, the variability of the flow between the shelf break and the EAUC is higher than the average flow, and the mean streamlines show smaller-scale eddy activity around this area (Fig. 7(d)). The stronger variability of the surface currents during July is also seen in the flow over the shelf, where the flow variability, especially closer to the shelf break, is higher than the mean flow.

Three additional features are apparent on the eastern end of the BoP, the East Cape area. First, on the eastern side of the East Cape, a cold water pool anomaly is present during both months. This feature is likely caused by tidal forcing interacting with the bathymetric extension of the East Cape, given that it is not present in the simulation without tides (Souza et al., 2022). Second, offshore just north of the East Cape, there is a region with strong flow variability present during both months. This region shows a strong outflow (>18 cm s^{-1}) that is channelled along the narrow East Cape shelf and transports water eastward out of the BoP. This feature will be referred to hereinafter as the East Cape Outflow (ECO). Finally, on the inner side of the East Cape, near Ōpōtiki, there is the presence of a recirculation zone close to the coast, between the coastline and the 65 m isobath. In this area, the mean streamlines show a recirculation around a region with low flow variability in both months.

To identify the impact of wind-driven upwelling circulation throughout three regions of the BoP (western, central and eastern), lagged cross-correlations for a 2-year period were calculated between shelf-oriented, low-pass filtered, along-shore wind stress and along-shore and cross-shore currents (Fig. 8). The cross-correlation between the along-shore wind stress and the along-shore currents shows that the central and western regions have a weak positive correlation throughout the water column, explaining up to 25 of the variability (Fig. 8(a)). Maximum correlation coefficient occurred with lag intervals of 15–18 h for the western region and 12–15 h for the central region (Fig. 8(b)), meaning that throughout the water column, the wind stress is leading the along-shore currents. Meanwhile, the eastern region has no significant correlation between the along-shore currents and the along-shore wind stress.

The cross-correlation between the along-shore wind stress and the cross-shelf currents shows that the near-surface currents (<10 m depth) in the three locations have a weak positive correlation. Between 10 and 30 m depth, there is a vertical shear marking the division between the upper Ekman layer, top boundary layer affected by the role of friction (wind forcing), and the bottom layer. Deeper cross-shelf currents (>30 m depth) negatively correlate to along-shelf wind stress. Up to 30 of the variability of the cross-shelf currents is explained by the variability of the along-shore wind stress (Fig. 8(c)). For the cross-shelf near-surface currents, the maximum correlation coefficient occurred with lag intervals of 3 h for the western region and −2 h for the central and eastern regions, rapidly reacting to the wind stress forcing (Fig. 8(d)). On deeper waters (>30 m depth), the correlation peak occurred with lag intervals of 20–23 h for the western region and 6–13 h for the central region.

The cross-correlation for the western and central regions illustrates an Ekman-driven upwelling and downwelling circulation. This shows the along-shore currents in the same direction as the along-shore wind stress and the cross-shore currents, with the near-surface flow to the left of the along-shelf wind stress and the near-bottom flow to the right. The differences in the dynamics between regions, with the eastern region showing no significant correlation to the along-shore wind stress, suggest a three-dimensional wind-driven flow, mainly due to variable coastline orientation. The wind forcing in the BoPM, obtained from CFSR, has a very uniform spatial structure. Therefore, the three-dimensional upwelling patterns in the BoP result from the variable coastline orientation relative to the principal axis component of the wind. The central and western regions are primarily aligned with the

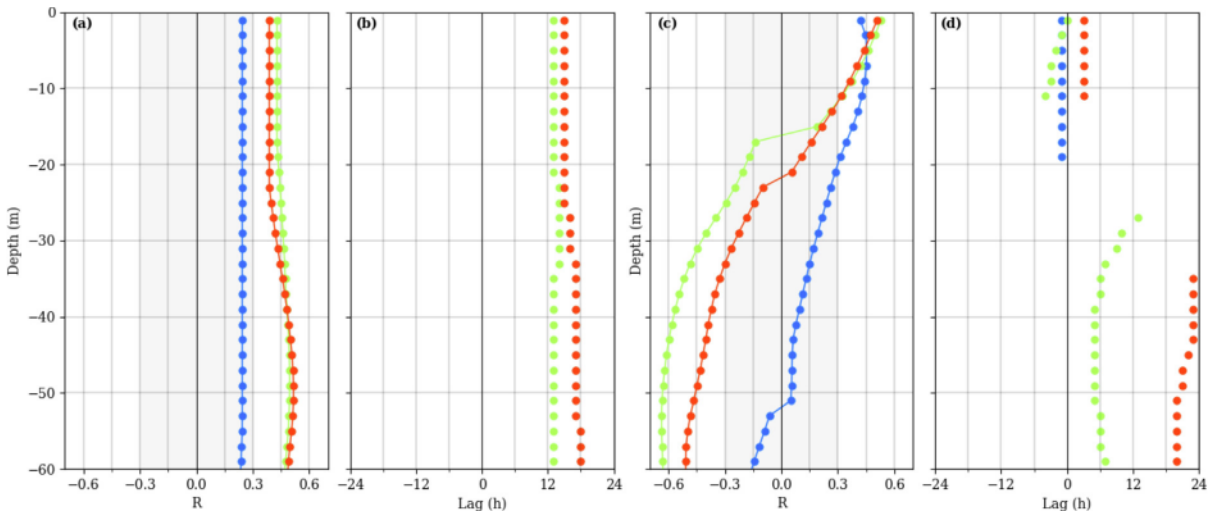

Fig. 8. Maximum lagged cross-correlation coefficients between along-shore wind stress and along-shore (a) and cross-shore (c) velocity components through the water column and associated lag intervals (b, d) at three locations representing the west (—), central (—) and east (—) region of the BoP during 2003–2004. The shadowed area delimits the non-significant correlation coefficients (95 confidence level) the associated lag values are not plotted. Negative lag indicates currents leading wind stress, and positive lag indicates wind stress leading currents.

wind due to the angle of the coastline. Meanwhile, the eastern region's coastline presents a different orientation followed by an abrupt change due to the presence of the East Cape. Lag intervals of the along-shelf wind stress to along-shelf flows throughout the water column on the western and central regions (15–18 h and 12–15 h, respectively) are close to the inertial period (19.6 h), suggesting a local response to the winds.

3.3. Lagrangian experiments

The Eulerian analyses provided the confidence that the simulated flow is realistic, therefore, a series of Lagrangian experiments were made to assess the pathways of the flow during different January and July atmospheric conditions and large-scale boundary current proximity. In particular, we are interested in how pathways and coastal mixing are affected in regions of the BoP and how they vary with distance offshore due to the influence of boundary currents. These experiments were modelled using the BoPM hourly output and OpenDrift, an open-source code programmed in Python for modelling the trajectories of objects, or substances, drifting in the ocean (Dagestad et al., 2018). The setup for these experiments included passive drifters advected offline and forward in time with a time-step of 900 s. These experiments use a fourth-order Runge–Kutta advection scheme and constant vertical and horizontal diffusivity values of 0.001, 0.1 $m^2\ s^{-1}$ respectively.

The experiments were done every month of the 2-year period for a total of 24 multi-release simulations. In each simulation, particles are advected for up to 30 days; during their drift, if a particle's position in the next time-step reaches a land-masked point, it strands and ceases its trajectory. Hereinafter these particles are referred to as stranded particles. Particles were released every 6 h, having a total of 112–124 releases depending on the length of the month. The particles are released over the continental shelf, delimited by the 200 m isobath, at different locations along the inner-shelf (20 m isobath, 31 locations), mid-shelf (65 m isobath, 27 locations), and the shelf break (200 m isobath, 27 locations) with a separation of ≈9 km in between each location (Fig. 9). These locations were defined to identify the interaction within the BoP regions and between the BoP shelf and the boundary currents. On each location, a cluster of 20 to 40 particles, depending on the isobath, were randomly placed in a 1 km radius and at variable depths throughout the water column. A total of 620, 810 and 1080 particles are released every 6 h.

To contrast BoP dispersal patterns during January and July conditions, Lagrangian Probability Density Functions (LPDF) after 30 days of advection of the releases were calculated (Fig. 9). The LPDF provides the spatial probability of finding a particle after a given advection time, giving an estimate of the dispersal pattern. For releases along the inner-shelf, the amount of stranded particles is 65 in January conditions and 76 in July conditions. Both conditions present high particle density areas along the coast, except for the Ōpōtiki area, which shows a relatively low particle density area more visible during July, and over the two islands near the coast, Moutohorā and Motiti Island (Figs. 9(a), 9(b)). During January conditions, the particles are distributed further from the coast along the shelf, having the outer islands, Tūhua and Whakaari, as moderate particle density areas and with 15 of the particles drifting over the continental shelf (Fig. 9(a)). During July conditions, only 5 of the particles drift over the continental shelf after 30 days. Meanwhile, the amount of particles that drift offshore is around the same order with 20 and 19 during January and July conditions, respectively. Although nearshore river inputs can influence coastal dispersion, due to the spatial resolution of the BoPM and because satellite imagery suggests that the width of river mouths across the BoP are mostly ≤1 km, these effects are not considered in our analysis.

For releases along the mid-shelf, the particle distribution is less concentrated along the coast, diminishing the number of particles stranded by half during January conditions by 28 . During these conditions, the high particle density areas are not along the coast but around the islands, with Tūhua Island as the highest particle density area, followed by Whaakari and Motiti Island (Fig. 9(c)). During July conditions, 37 of particles are stranded, and the highest particle density areas are located around the central and western coast of the BoP (Fig. 9(d)). The amount of particles drifting over the continental shelf after 30 days is at least doubled, compared to the inner-shelf reported values, with 30 in January conditions, showing a more extended and relatively even distribution over the continental shelf, and 14 in July conditions. Meanwhile, 42 and 49 of the particles drift offshore during January and July conditions, respectively.

For near-shelf break releases, the amount of particles that get stranded diminishes to 11 during January and July conditions. For these releases, the outer islands, Tūhua and Whakaari, are high particle density areas. During January conditions, there is an eastward and more constrained distribution close to the shelf break having 27 of particles drifting over the continental shelf and 62 of particles

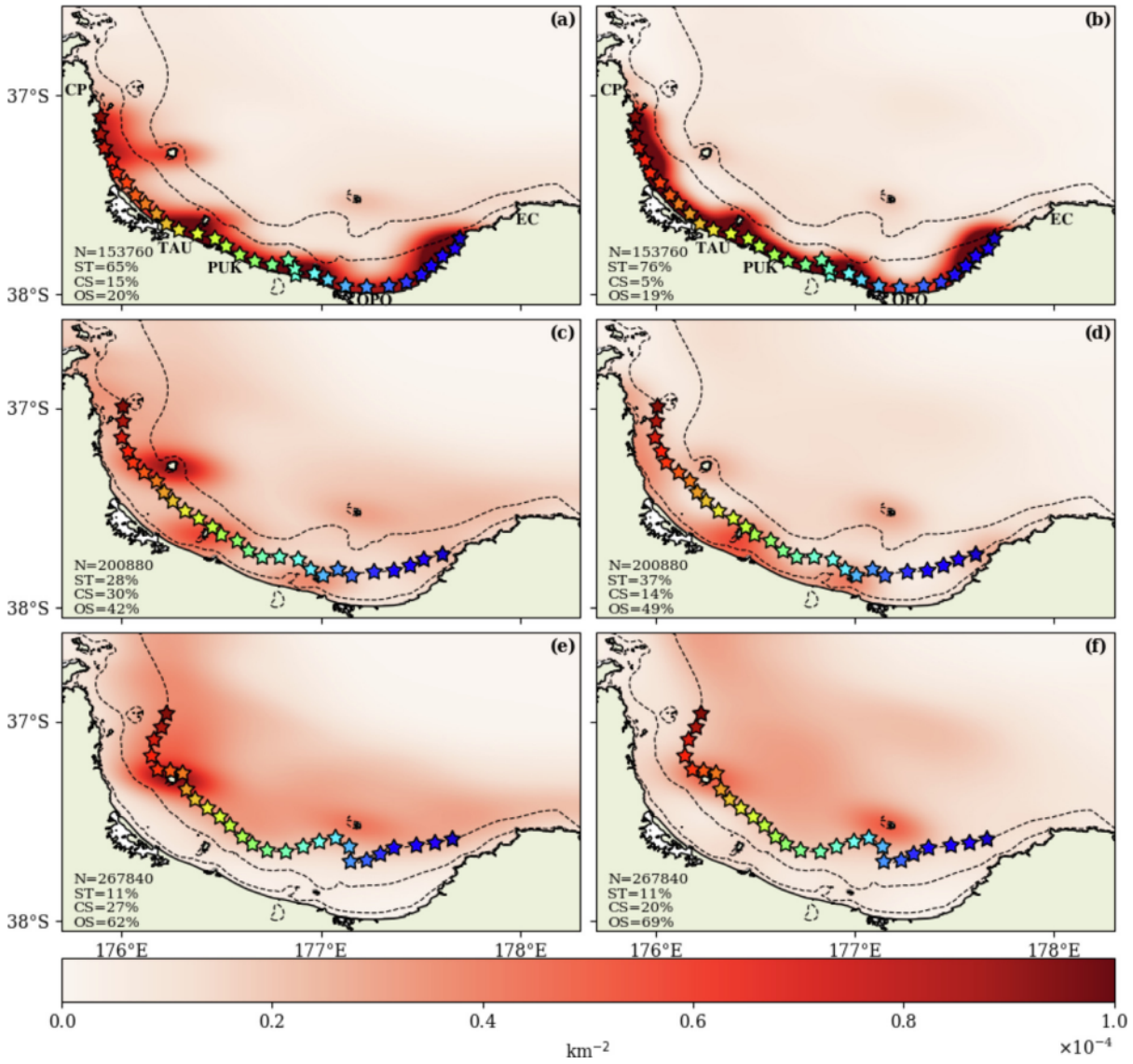

Fig. 9. Zoom in of the horizontal Lagrangian probability density function (km^{-2}) after 30 days of advection for the inner-shelf (a, b), mid-shelf (c, d) and shelf break (e, f) releases during the January (a, c, e) and July (b, d, f) conditions for the years 2003–2004. The coloured stars ( ) represent the different release locations, with blue colours indicating the most eastward locations and red colours indicating the most westward locations. The dashed lines (– – ·) represent the 20, 65, and 200 m isobath. Let N be the total number of particles, ST the stranded particles ( ), CS the particles over the continental shelf (, <200 m isobath), and OS the particles offshore (, >200 m isobath). (For interpretation of the references to colour in this figure legend, the reader is referred to the web version of this article.)

drifting offshore (Fig. 9(e)). Meanwhile, during July conditions, there is an upstream, offshore, and more dispersed distribution offshore, having 69 of particles offshore and 20 of particles drifting over the continental shelf (Fig. 9(f)). These near-shelf break releases have the most similar values in between conditions.

During January conditions, the surface patterns show that the inner-shelf and mid-shelf releases are getting distributed further from shore, aligning with an upwelling-driven circulation dynamic following the Ekman transport (Figs. 9(a), 9(c)). The vertical PDF of the mid-shelf releases shows that the particles during January conditions are more likely to be distributed at the surface over the pycnocline (Figs. 10(b)–10(a)). Meanwhile, the vertical and horizontal distribution is more variable during July conditions, similar to the winds. High particle density areas are present with more dispersion throughout the BoP region (Figs. 9(d), 9(f)). In the vertical, the average profile of potential density shows that during July conditions, the water column is strongly mixed, characteristic of a winter month with event-scale storm systems that tend to deepen the mixed layer through wind-driven mixing (Fig. 10(a)). The vertical PDF of the mid-shelf releases shows that the particles during July conditions have a more variable distribution, consistent with the strongly mixed water column, having ≈45 of particles distributed below 100 m depth (Fig. 10(b)). The LPDFs show that after 30 days of advection, there is more variability represented during July conditions (Figs. 9(b), 9(d), 9(f)) compared to the more limited horizontal dispersal distribution of particles during January conditions (Figs. 9(a), 9(c), 9(e)). The contrast between January and July mirrors the estimated mean circulation patterns during these conditions (Fig. 7).

To complement the LPDFs, and to have a preliminary qualitative distinction of the trajectories between regions and time scales, a brief description of the pathways along the BoP under two wind-forcing conditions after 7 and 30 days is given (Figs. 11 and 12). To minimise trajectory overlap, only every 5th particle is plotted. Trajectories are plotted sequentially by location, from east to west (blue to red), for every 12th release time (n = 124). After 7 days of advection, under January conditions, the nearshore flow shows a southeastward tendency for most of the regions except for the most western released particles (Figs. 11(a), 11(c)). Along the inner-, mid-shelf and shelf break releases,

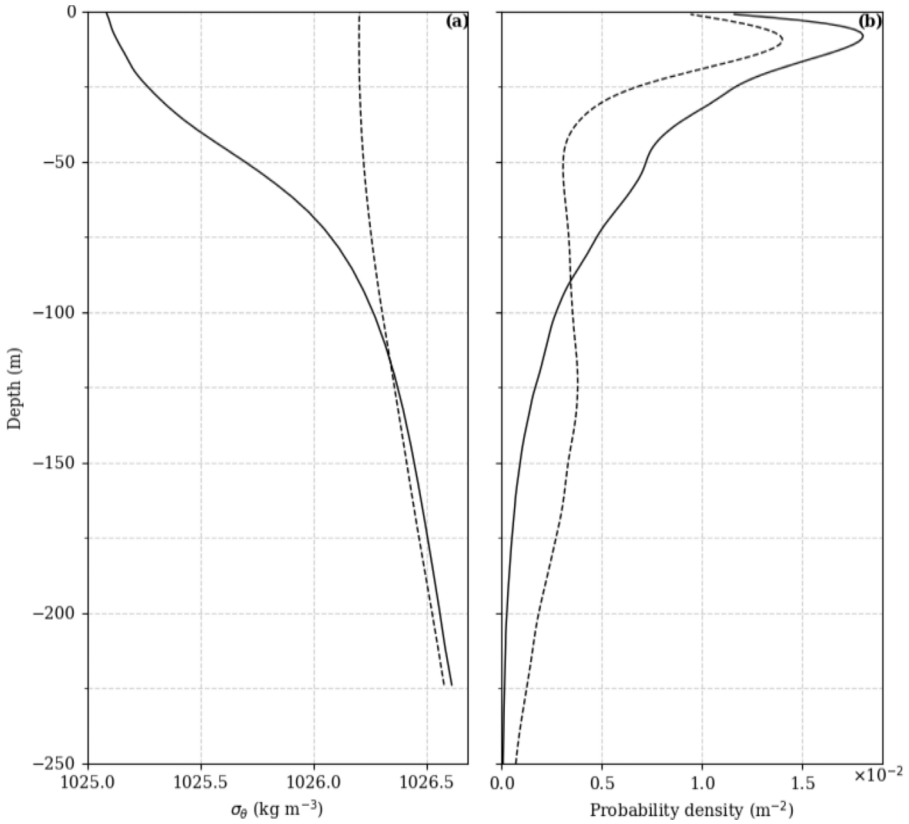

Fig. 10. (a) Average profile of potential density (σ_θ, kg m^{-3}) for January (——) and July (– – ·) conditions near the shelf break for the central BoP (Pukehina) for the year 2003–2004. (b) Vertical probability density function (m^{-2}) after 30 days of advection of along the mid-shelf releases during January (——) and July (– – ·) conditions for the year 2003.

the most eastern released particles get rapidly entrained into the EAUC (Figs. 11(a), 11(c), 11(e)). Under July conditions, the inner- and mid-shelf releases do not show one clear outflow pathway through the bay, there appears to be a convergence towards areas where the shelf break widens from the coast. This is clear towards Whaakari Island, where the isobaths diverge and lead to flow separation that carries inner-shelf released particles offshore (Fig. 11(b)). Due to the offshore position of the EAUC, there is eddy activity near the shelf break. Particles are seen to become entrained in these eddies and are retained near the mouth of the BoP (Figs. 11(d), 11(f)). After 7 days under both conditions, there is a separation between the western, central and eastern released particles, especially in the inner- and mid-shelf releases. The particles interact with adjacent regions, but there is an apparent limited interaction between the western and eastern regions. After 30 days of advection, the impact of the mesoscale features is more evident, especially for the along mid-shelf and shelf break releases (Fig. 12). During January conditions, Lagrangian particles released along the inner-, mid- and shelf break follow a south-east flow and get entrained into the EAUC and ECE (Figs. 12(a), 12(c), 12(e)). Meanwhile, during July conditions, Lagrangian trajectories show similar patterns to those shown after 7 days. The Lagrangian particles stay relatively close to the shelf break, showing a more variable eddy motion flow and stronger mixing offshore between the western, central, and eastern regions (Figs. 12(b), 12(d), 12(f)). As seen on the particle trajectories after 7 days, after 30 days, there is limited interaction between the nearshore western and eastern regions. One notable exception is during January conditions, western released particles can reach the eastern region taking a complicated pathway, they have to leave the shelf and re-enter from the east (Figs. 12(a), 12(c), 12(e)). During July conditions, there is no evident interaction between the eastern and western nearshore regions.

4. Discussion

4.1. Mesoscale and wind-driven circulation in comparison to previous studies

The monthly averages showed variability in the position and strength of the mesoscale features (Fig. 7), the EAUC and the ECE, consistent with what was reported on previous studies done over larger scales and northeast shelf of Aotearoa New Zealand (Stanton et al., 1997; Roemmich and Sutton, 1998; Stanton and Sutton, 2003; Zeldis et al., 2004; Fernandez et al., 2018). The stronger mean flow of the EAUC during January (25–30 cm s^{-1}) relative to July (20–25 cm s^{-1}) is consistent with the stronger transport during summer and weaker during winter for the entirety of the EAUC reported by Fernandez et al. (2018) using along-track altimetry. The EAUC proximity to shore during January has been previously reported as a shoreward progression of the EAUC offshore of the Hauraki Gulf (Zeldis et al., 2004; Santana et al., 2021). The area surrounding the ECE has been described as a region with extremely high variability (Roemmich and Sutton, 1998; Tilburg et al., 2001). Roemmich and Sutton (1998) identified the centre of the ECE at 178.2°E, 36.2°S with variations in the position of the ECE. Altimetric snapshots during February 1995 showed a stronger and slightly closer-to-shore ECE, while during June 1994, they showed an ECE located further from shore. Although our findings are consistent with previous studies, most of these are done over a relatively short period. Silva et al. (2019) stated that there is substantial evidence of interannual variability in the BoP. The BoPM can hopefully be a valuable tool for future studies on the interannual variability of the BoP coastal region.

The BoPM produces wind-driven Ekman-like dynamics around the western and central BoP with along-shelf currents in the along-shelf wind stress direction and near-surface flow heading off-shore, and

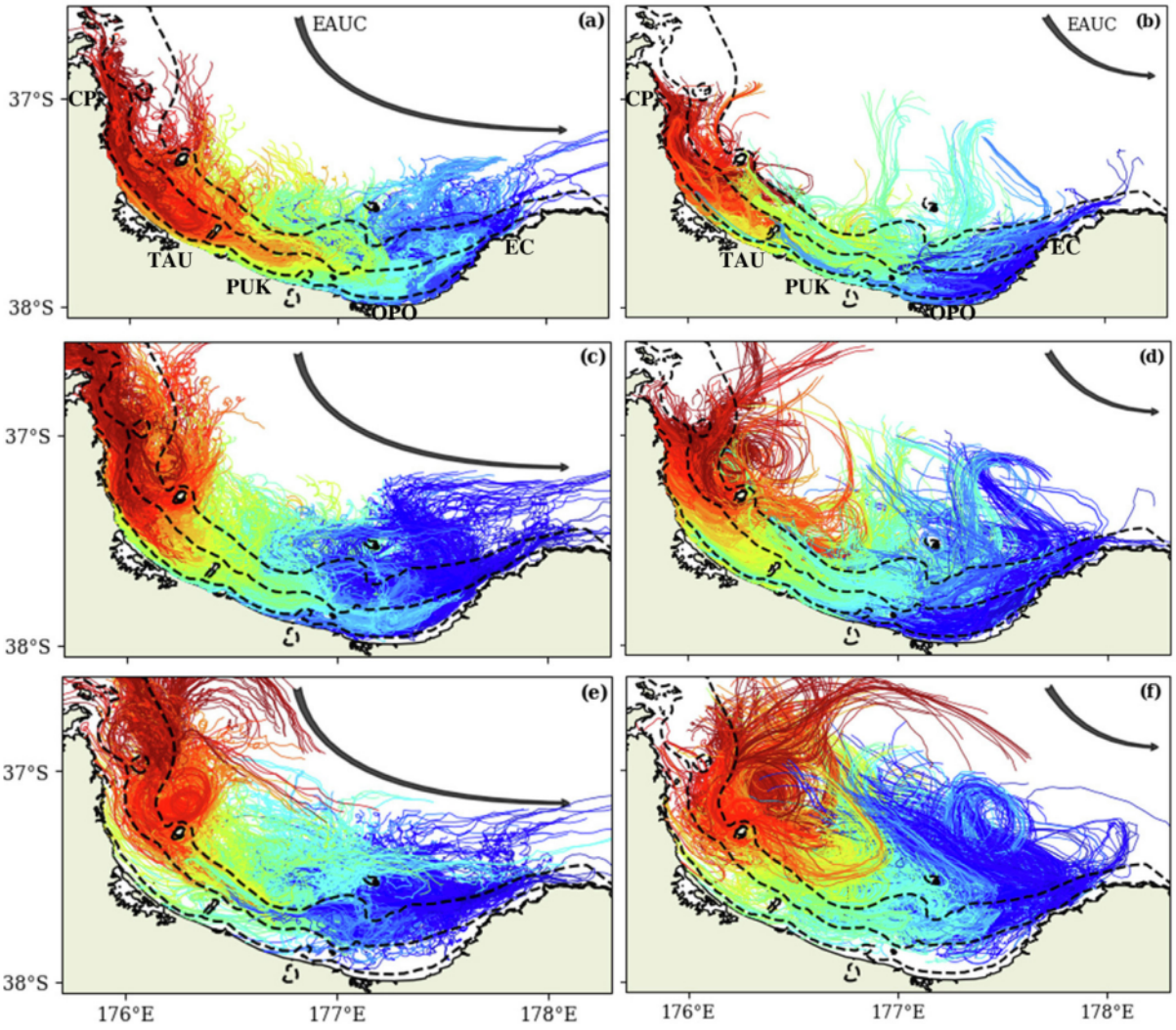

Fig. 11. Zoom in of the Lagrangian trajectories after being advected for 7 days for each release location along the inner-shelf (a–b), mid-shelf (c–d) and shelf break (e–f) during January (a, c, e) and July (b, d, f) conditions. The colours represent the different release locations, blue indicating the most eastward locations and red indicating the most westward locations. The exact release locations can be seen on Fig. 9. The dashed lines (– – ·) represent the 20, 65, and 200 m isobath. The arrows ( ) are the schematic representation of the EAUC as seen on Figs. 7(a)–7(b). (For interpretation of the references to colour in this figure legend, the reader is referred to the web version of this article.)

near-bottom flow heading shorewards (Fig. 8). This wind-driven upwelling dynamic has been previously reported on an event time scale by Longdill (2008) within the central BoP and by Sharples and Greig (1998) and Zeldis et al. (2004) for the Northeastern region of Aotearoa New Zealand. The variability explained by the cross-correlation between the along-shore wind stress and the along-shore currents (up to ≈25) and the cross-shore currents (up to ≈30) is lower than the 35 –41 and 25 –35 , respectively, observed by Longdill et al. (2008), and the maximum of ≈36 reported by Zeldis et al. (2004). The explained variability in the model is less than the previously observed by Longdill et al. (2008) because our analysis spans an entire 2-year period. Wind-driven upwelling is more relevant on an event-scale, but non-wind-driven mechanisms are more important on longer time scales. The cross-shelf velocities rapidly respond to along-shelf wind stress on the western and central regions, similar to other upwelling regions (Cushman-Roisin et al., 1983; Zeldis et al., 2004; Longdill et al., 2008). Whereas the lag intervals reported for the along-shore flows throughout the water column (15–18 h and 12–15 h) and the deep cross-shore flows (21–23 h and 6–13 h) to along-shelf wind stress in the western and central regions are on a similar range to the reported by Longdill et al. (2008). These results suggest that the model correctly simulates the local response to the winds.

The eastern region of the BoP shows a reduced local wind-forcing influence, suggesting that other non-wind-driven mechanisms are more dominant. The mean circulation in this region shows a reversal of along-shore flow (Fig. 7), suggesting a recirculation due to the presence of the East Cape headland downwind. Following Largier (2020), the BoP can be classified as a wide-open step bay where along-shore winds can result in a cyclonic circulation feature and retention of waters over the inner-shelf. This has been observed in studies of coastal regions in the lee of a small headland (e.g., Roughan et al., 2005) and on a larger scale where higher larval settlement is associated with headland embayments (Wing et al., 1995).

4.2. Lagrangian statistics and coastal retention

As defined by LaCasce (2008), Lagrangian statistics support the preliminary qualitative description given in Section 3.3. The total absolute dispersion reflects the spread about the centre of mass and the drift from the starting location ($A^2\rangle$, single particle statistic). Let $x_n(t)$ and $y_n(t)$ be the along-shore and cross-shore position of a particle that remains in the water at a time since release t. The total absolute dispersion is given by:

$$A^2(t)\rangle = [x_n(t) - x_n(t_0)]^2 + [y_n(t) - y_n(t_0)]^2\rangle \quad (4)$$

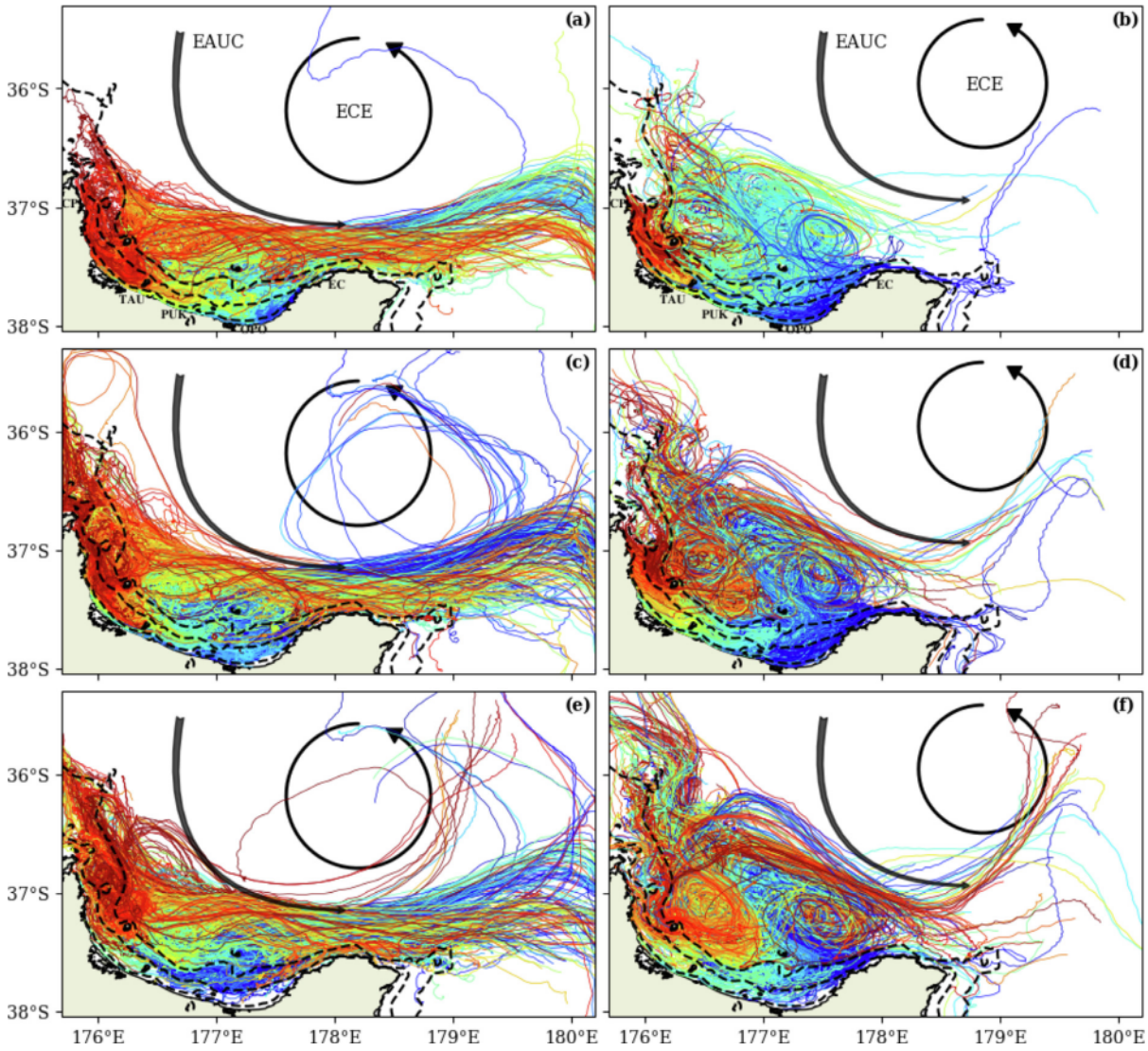

Fig. 12. Lagrangian trajectories after being advected for 30 days for each release location along the inner-shelf (a–b), mid-shelf (c–d) and shelf break (e–f) during January (a, c, e) and July (b, d, f) conditions. The colours represent the release locations; blue indicates the most eastward locations, and red indicates the most westward locations. The exact release locations can be seen on Fig. 9. The dashed lines (– – ·) represent the 20, 65, and 200 m isobath. The arrows ( ) are the schematic representation of the EAUC and ECE as seen on Figs. 7(a)–7(b). (For interpretation of the references to colour in this figure legend, the reader is referred to the web version of this article.)

where ⟩ denotes an average and $x_n(t_0)$ $y_n(t_0)$ is the initial position of the particle. The relative dispersion (R^2⟩, two-particle statistic) reflects how a cloud of tracer spreads about its centre of mass as a function of time. Let $x_m(t)$, $y_m(t)$ and $x_n(t)$, $y_n(t)$ be the along-shore and cross-shore position of two drifters from the same group of particles initially separated by a given distance X_0 at time t. The total relative dispersion for a group of particles, where m n, is given by

$$R^2(t\ X_0)\rangle = \ [x_m(t) - x_n(t)]^2 + [y_m(t) - y_n(t)]^2\rangle \quad (5)$$

During January conditions, the eastern released particles show a faster absolute dispersion during the first 7 days, while the absolute dispersion from the particles released over the western region is smaller (Figs. 13(a)–13(c)) consistent with the observed on the Lagrangian trajectories where eastern particles were getting entrained into the EAUC circulation early on (Figs. 11(a), 11(c), 11(e)). It takes between 9–15 days, depending on the release location, for particles released on the inner-shelf to reach a distance that covers the area of the bay (9.6×10^3 km^2), meaning that depending on the release location it can take up to 15 days for a particle to travel the entirety of the BoP. After 30 days, the eastern locations' absolute dispersion is lower compared to the western and central locations for the inner-shelf releases. Meanwhile, the shelf break releases show fewer differences between locations after 30 days.

Table 3
Best-fit of a power law growth for the average relative dispersion ($R^2(t)$)) between day 1 through 10 and between day 15 through 30 during January and July conditions.

	1–10 days		15–30 days	
	January	July	January	July
Release m)				
Inner-shelf	$t^{2.5}$	$t^{2.5}$	$t^{1.5}$	$t^{2.3}$
Mid-shelf	$t^{2.2}$	$t^{2.0}$	$t^{1.4}$	$t^{2.0}$
Shelf break	$t^{2.0}$	$t^{1.7}$	$t^{1.3}$	$t^{1.7}$

The changes in the relative dispersion growth through time can help distinguish between ballistic ($R^2 \approx t^2$) and diffusive regimes ($R^2 \approx t^1$). Here we compare average rates of change for all release locations with these conceptual regimes of dispersion (Table 3). The relative dispersion during January conditions suggests two growth phases. During the first 10 days, inner-shelf releases show growth of $t^{2.5}$, this growth decreases for the mid-shelf ($t^{2.2}$) and shelf break releases ($t^{2.0}$),

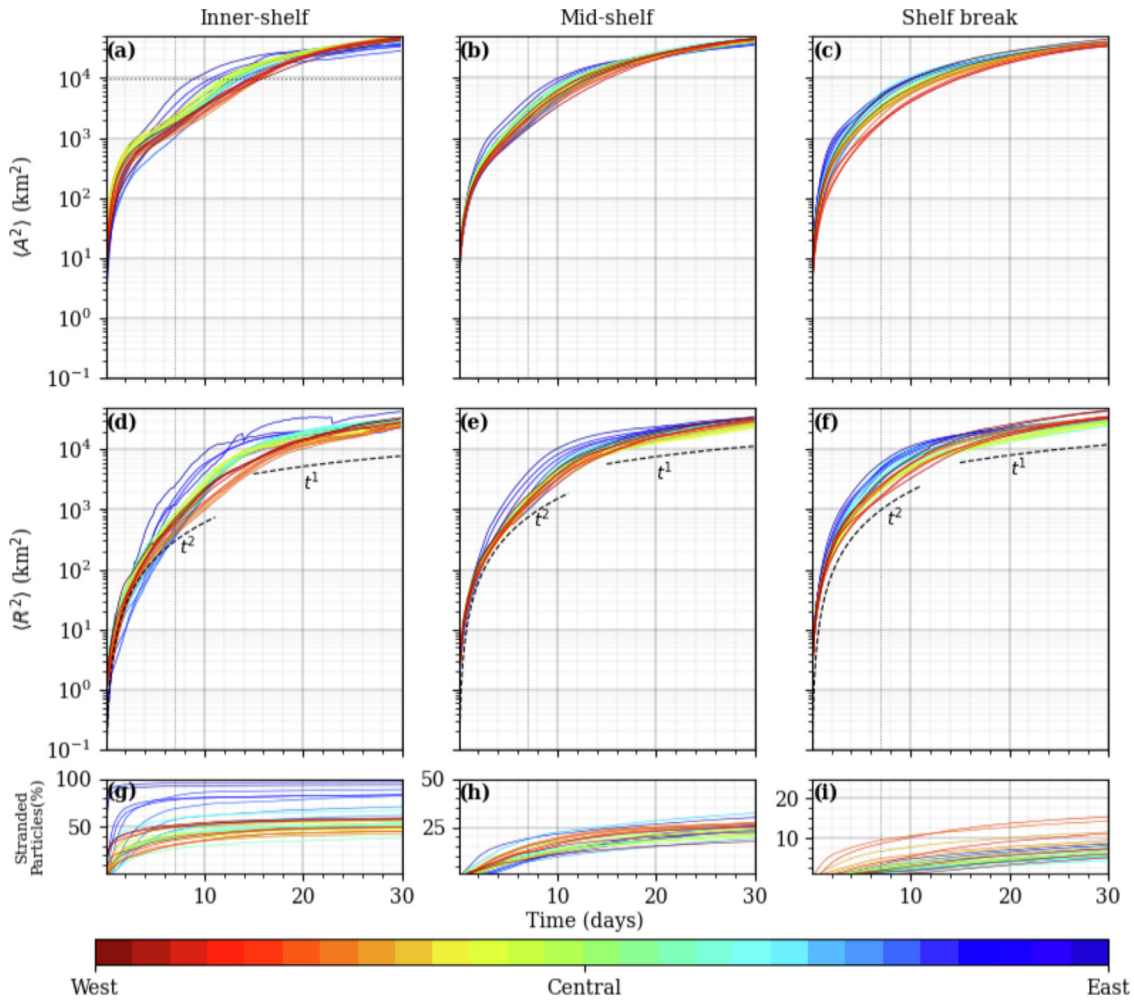

Fig. 13. (a–c) January conditions average of the single-particle dispersion (A^2) (km^2)) of the particle release experiment at the inner-shelf (a), mid-shelf (b) and shelf break (c). (d–f) January conditions average of the relative dispersion (R^2) (km^2)) of the particle release experiment at the inner-shelf (d), mid-shelf (e) and shelf break (f). The black dashed lines are a reference to the average power laws. (g–i) Percentage of the January conditions average amount of particles stranded on a 30-day period. The colours indicate where along the coast the particles were released; blue colours indicate the most eastern locations, and red colours indicate the most western locations. The exact release locations are indicated on Fig. 9. (For interpretation of the references to colour in this figure legend, the reader is referred to the web version of this article.)

suggesting a ballistic regime. After 15 days, inner-shelf releases show growth of $t^{1.5}$ and decreased power law growth for the mid-shelf ($t^{1.4}$) and shelf break releases ($t^{1.3}$) closer to the diffusive regime growth rate. The presence of these two regimes, a ballistic regime that transitions to a diffusive regime, has been seen previously in coastal areas. For example, Haza et al. (2008) found relative dispersion with a rate of $t^{0.7}$ after 30 days with virtual drifters in the Adriatic Sea, Beron-Vera and LaCasce (2016) and Sansón et al. (2017) found a linear growth of the relative dispersion for observed drifters after 20 days in the Gulf of Mexico.

During July conditions, particles show a slightly smaller absolute dispersion after 30 days relative to January conditions (Figs. 14(a)–14(c)). Similar to January conditions, the eastern locations of the inner-shelf releases show a faster dispersion rate during the first 7 days compared to the western locations, but after 30 days, the dispersion in between regions is similar. During July conditions, particles released on the inner-shelf take between 12–20 days to reach a distance that covers the area of the bay (9.6×10^3 km^2), showing a slower rate to travel the entirety of the BoP. The differences between regions are less visible during July conditions for the mid-shelf and shelf break releases.

In contrast with January conditions, the relative dispersion during July conditions maintains growth of $t^{2.5}$, $t^{2.0}$ and $t^{1.7}$, for the inner-, mid-shelf and shelf break releases, respectively, throughout the 30-day period (Table 3, Figs. 14(d)–14(f)). This has been reported by LaCasce and Ohlmann (2003) using observed drifters in the Gulf of Mexico where the relative dispersion maintained a power law growth of $t^{2.2\pm0.8}$ evident for up to 50 days. They suggested two possible explanations, shear dispersion and inverse energy cascade, stating that neither could be ruled out, as they might be happening simultaneously. Moreover, Callies et al. (2015) observed that submesoscale flows in the Gulf Stream region are much stronger during winter than in summer. Even though the BoP presents lateral shear due to the EAUC, this current is located further from shore during July conditions. This suggests that the relative dispersion ballistic regime at late times during July is due to strong mixing in the BoP associated with submesoscale processes resolved by the BoPM.

In our study, we are able to resolve differences in dispersion and stranding between releases along and across the bay. Under both defined atmospheric conditions, the pairs of particles released on the eastern region, especially along the inner-shelf, present a higher power law growth compared to the western and central released particles. Romero et al. (2013) defined that headlands are more dispersive and energetic than bays. Considering this, the central and western regions can be classified as bays, while the eastern region can be classified as a headland. These differences between regions are reduced when the releases are done further from the coast, especially during winter. However, note that only freely-drifting particles are considered in these dispersion statistics (Figs. 13(g)–13(i), 14(g)–14(i)). As particles strand during their trajectory, they are removed from the dispersion estimates. As

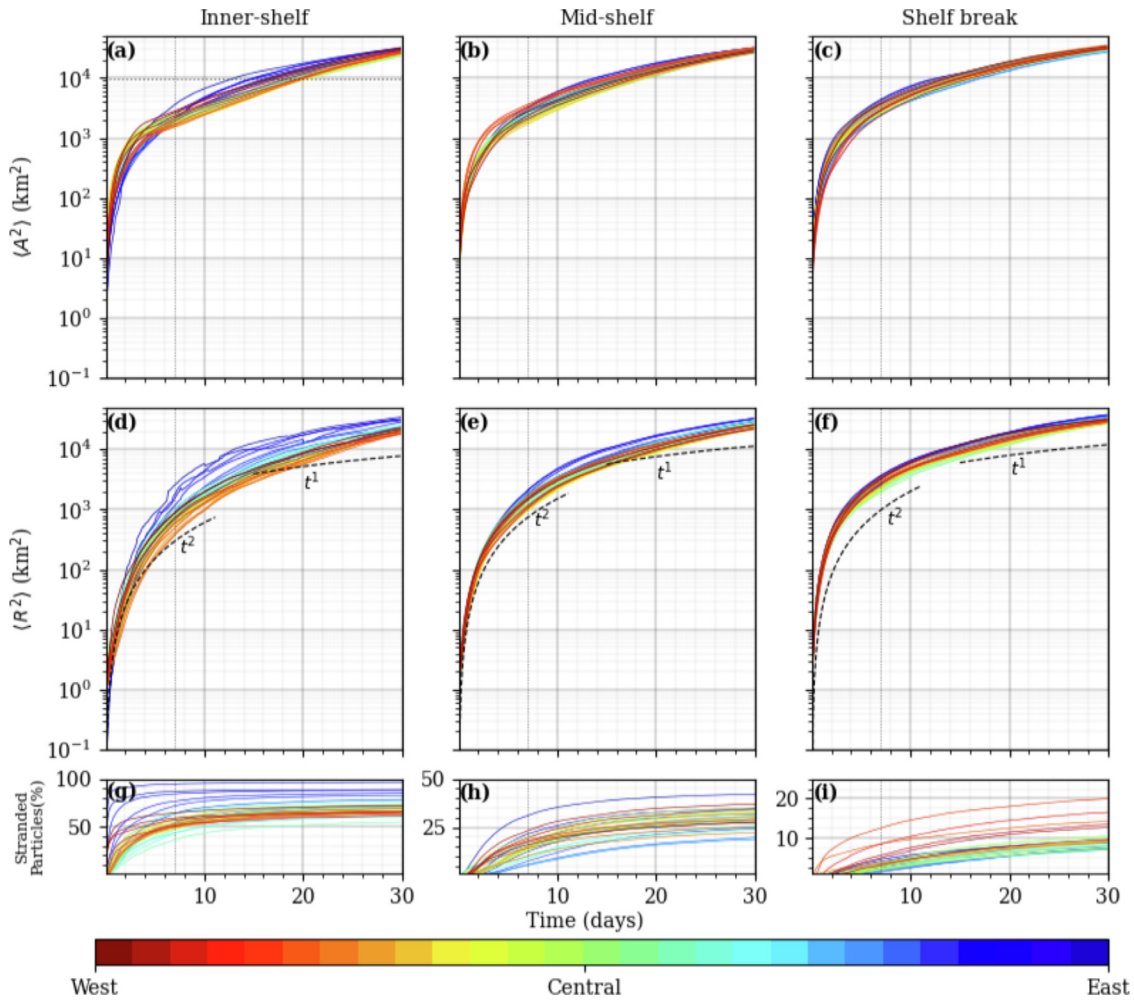

Fig. 14. (a–c) Single-particle dispersion average (A^2⟩ (km^2)) of the particle release experiment under July conditions at the inner-shelf (a), mid-shelf (b) and shelf break (c). (d–f) Relative dispersion average (R^2⟩ (km^2)) of the particle release experiment under July conditions at the inner-shelf (d), mid-shelf (e) and shelf break (f). The black dashed lines are a reference to the average power laws. (g–i) Percentage of the July conditions average amount of particles stranded on a 30-day period. The colours indicate where along the coast the particles were released; blue colours indicate the most eastern location, and red colours indicate the most western locations. The exact release locations can be seen on Fig. 9. (For interpretation of the references to colour in this figure legend, the reader is referred to the web version of this article.)

seen on the LPDFs, more particles are stranded during July compared to January conditions overall on the BoP. The eastern side of the BoP is a downwind region where the particle drift duration is ≈ five days for 70 –90 of the particles (Figs. 13(g), 14(g)). The high percentage of stranded particles suggests this region acts as a retention zone, consistent with the previous result from the Eulerian fields (Section 3.2). With the presence of an open-water mussel farm in this region of the BoP, the retention zone could limit larval dispersion and benefit local mussel abundance. The percentage of stranded particles reduces to ≈15 –30 and less than 20 , for the mid-shelf and shelf break releases respectively (Figs. 13(h)–13(i), 14(h)–14(i)). For the mid-shelf releases, there is no clear distinction between regions. For the shelf break releases, the western locations are the ones that present more stranded particles. As seen on the LPDFs, the further from the coast the releases are, the less amount of particles that get stranded along the coast, and the more relevant islands are as receiving regions. This is consistent with the stated by Mitarai et al. (2009) for the Southern California Bight, where islands functioned more importantly as inland particle receptors.

5. Summary and conclusions

In this study, three key elements were addressed: (1) the evaluation of a high-resolution simulation (BoPM), with realistic atmospheric, tidal and boundary forcings over a 2-year period (Section 3.1), (2) the wind-driven circulation and the mean circulation patterns of the Bay of Plenty under two different atmospheric forcing conditions (Sections 3.2 and 4.1), (3) the Lagrangian aspects of the flow along and across the Bay of Plenty under two different atmospheric forcing conditions (Sections 3.3 and 4.2).

The BoPM is a 28-year uninterrupted simulation, with a 1 km horizontal resolution, 50 sigma-levels, well-resolved coastline, high-resolution bathymetry and inclusion of 4 islands. The BoPM evaluation demonstrated good model skill in reproducing the ocean water temperature, sea level and water column velocity variability over tidal and non-tidal timescales. The salinity is mostly well reproduced over the BoP domain. During winter and extreme flooding events, the lack of riverine influence is particularly noticeable in near-shore locations (10–20 m isobath). The BoPM outperforms the Moana Ocean Hindcast (parent grid) in the coastal and offshore regions, suggesting that submesoscale processes impact the large-scale circulation over the region. A further step in improving the BoPM could be to simulate river discharge into the coastal ocean at a higher resolution. Alternately, higher-resolution atmospheric forcing might also be beneficial (Myksvoll et al., 2012; Goubanova et al., 2019). The current simulation provides a baseline to analyse the ocean dynamics in the coastal region of the BoP, taking into account submesoscale processes unresolved in a regional model.

The BoPM showed the ability to reproduce the variability of the mesoscale features. January conditions showed a stronger EAUC and an EAUC and ECE closer to the shelf. July conditions indicated that the EAUC and ECE are located further from the shelf. Both presented scenarios are consistent with previous observations. This shows that the BoPM can be a valuable tool for studying the presence of seasonal, interannual and/or annual cycles and long-term trends of the mesoscale features and their influence on coastal circulation.

The BoPM also showed the ability to reproduce wind-driven circulation, analysing a 2-year period using cross-correlations between the along-shore wind stress and the along-shore and cross-shore currents. The cross-correlation analysis over the western and central regions of the BoP explains up to ≈30 of the variability. The lag intervals, ranging between 15–18 h and 12–15 h for the western and central regions, respectively, are close to the inertial period (19.6 h), suggesting that the model correctly represents the response to local winds. The upwelling wind-driven Ekman dynamics in this region are due to coastline orientation relative to wind direction. However, the eastern region shows no significant correlation between the along-shore wind stress and the along- and cross-shore currents suggesting a three-dimensional wind-driven flow along the bay. Further studies are needed to identify the variability explained by non-wind-driven forcings.

The Lagrangian trajectories and statistics were contrasted under two wind-forcing conditions. January conditions, predominantly upwelling-favourable winds, presented two dispersion regimes, a ballistic regime ($R^2 \approx t^2$) over the first 10 days followed by a diffusive regime ($R^2 \approx t^1$) after 15 days. Under July conditions, stronger and more variable winds, the diffusive regime was never reached, maintaining a ballistic regime with the same power law growth throughout 30 days, likely due to an inverse energy cascade. The distance from the shore of the releases plays a role in the dispersion. The further from shore the releases are, the more influence from mesoscale features they get. Under January conditions, the releases further from shore show a lower power law growth of $t^{2.5}$, $t^{2.2}$ and $t^{2.0}$ for the inner-, mid-shelf and shelf break releases, respectively. This is also present under July conditions, with power-law growth values of $t^{2.5}$, $t^{2.0}$ and $t^{1.7}$ for the inner-, mid-shelf and shelf break releases, respectively. The differences between regions are smaller under July conditions relative to January conditions. Overall, the eastern-released particles show a higher power law growth relative to the western-released particles. This higher dispersion is associated with the proximity to the headland and the ECO. Even though the eastern released particles show a higher power law growth under both conditions, these locations present a particle drift duration of ≈5 days for 70 –90 of the particles along the inner-shelf releases. These results suggest the presence of a retention zone, retaining material by carrying particles towards the coast. For the mid-shelf and shelf break releases, the islands function more importantly as receptors of particles. Future studies are needed to increase the understanding of the connectivity between regions through the BoP.

A realistic, coastal-resolving, long-term simulation of the Bay of Plenty can have important future implications. This model can be used to serve Bay of Plenty coastal waters as boundary conditions for higher resolution models that simulate the multiple estuaries found around the bay and/or to include the effects of surface gravity waves or to evolve into an operational forecast model, both are current aspirations of the Moana Project on a local scale. The reported results provide useful information to start unravelling the processes that occur in the BoP, identifying differences between the western, central and eastern regions and contrasting two atmospheric forcings. A better understanding of these oceanographic processes can benefit surrounding communities in the form of improved management practices and/or emergency response situations.

CRediT authorship contribution statement

Mireya M. Montaño: Writing – original draft, Visualization, Validation, Methodology, Investigation, Formal analysis, Conceptualization. **Sutara H. Suanda:** Writing – review & editing, Supervision, Conceptualization, Methodology, Resources.. **João Marcos Azevedo Correia de Souza:** Writing – review, Resources.

Declaration of competing interest

The authors declare the following financial interests/personal relationships which may be considered as potential competing interests: Mireya Montano reports financial support was provided by New Zealand Ministry of Business Innovation and Employment.

Data availability

The dataset will become available in the future on the project page, but at the moment is available upon request.

Acknowledgements

This work is a contribution to the Moana Project (www.moanaproject.org), funded by the New Zealand Ministry for Business Innovation and Employment, contract number METO1801. We acknowledge Peter Longdill, the Bay of Plenty Regional Council, the Land Information New Zealand (LINZ) and NIWA for collecting and providing measurements throughout the Bay of Plenty, John Wilkin for advice in BoPM model configuration, Moninya Roughan for securing the funding and conceptualising the Moana Project and He Hono Moana group for valuable interdisciplinary discussions. We also acknowledge the reviewers for their comments, corrections and suggestions that have improved this paper.

References

Babiano, A., Basdevant, C., Le Roy, P., Sadourny, R., 1987. Single-particle dispersion, Lagrangian structure function and Lagrangian energy spectrum in two-dimensional incompressible turbulence. J. Mar. Res. 45 (1), 107–131. http://dx.doi.org/10.1357/002224087788400936.

Beckmann, A., Haidvogel, D.B., 1993. Numerical simulation of flow around a tall isolated seamount. part I: Problem formulation and model accuracy. J. Phys. Oceanogr. 23 (8), 1736–1753. http://dx.doi.org/10.1175/1520-0485(1993)023<1736:NSOFAA>2.0.CO;2.

Beron-Vera, F.J., LaCasce, J.H., 2016. Statistics of simulated and observed pair separations in the gulf of Mexico. J. Phys. Oceanogr. 46 (7), 2183–2199. http://dx.doi.org/10.1175/JPO-D-15-0127.1.

Black, K.P., Beamsley, B., Longdill, P.C., Moores, A., 2005. Bay of Plenty Current and Temperature Measurements: Aquaculture Management Areas. Data Report, ASR Ltd, Raglan New Zealand, p. 67, URL: https://atlas.boprc.govt.nz/api/v1/edms/document/A3888450/content.

Callies, J., Ferrari, R., Klymak, J.M., Gula, J., 2015. Seasonality in submesoscale turbulence. Nature Commun. 6 (1), 6862. http://dx.doi.org/10.1038/ncomms7862.

Chin, T.M., Vazquez-Cuervo, J., Armstrong, E.M., 2017. A multi-scale high-resolution analysis of global sea surface temperature. Remote Sens. Environ. 200, 154–169. http://dx.doi.org/10.1016/j.rse.2017.07.029.

Chiswell, S.M., Rickard, G.J., 2011. Larval connectivity of harbours via ocean currents: A New Zealand study. Cont. Shelf Res. 31 (10), 1057–1074. http://dx.doi.org/10.1016/j.csr.2011.03.012.

Choi, J., Bracco, A., Barkan, R., Shchepetkin, A.F., McWilliams, J.C., Molemaker, J.M., 2017. Submesoscale dynamics in the northern gulf of Mexico. part III: Lagrangian implications. J. Phys. Oceanogr. 47 (9), 2361–2376. http://dx.doi.org/10.1175/JPO-D-17-0036.1.

Cowen, R.K., Paris, C.B., Srinivasan, A., 2006. Scaling of connectivity in marine populations. Science 311 (5760), 522–527. http://dx.doi.org/10.1126/science.1122039.

Cushman-Roisin, B., O'Brien, J.J., Smith, R.L., 1983. On wind and ocean-velocity correlations in a coastal-upwelling system. J. Phys. Oceanogr. 13 (3), 547–550. http://dx.doi.org/10.1175/1520-0485(1983)013<0547:OWAOVC>2.0.CO;2.

Dagestad, K.-F., Röhrs, J., Breivik, Ø., Ådlandsvik, B., 2018. OpenDrift v1.0: A generic framework for trajectory modelling. Geosci. Model Dev. 11 (4), 1405–1420. http://dx.doi.org/10.5194/gmd-11-1405-2018.

Dee, D.P., Balmaseda, M., Balsamo, G., Engelen, R., Simmons, A.J., Thépaut, J.-N., 2014. Toward a consistent reanalysis of the climate system. Bull. Am. Meteorol. Soc. 95 (8), 1235–1248. http://dx.doi.org/10.1175/BAMS-D-13-00043.1.

Dong, C., McWilliams, J.C., 2007. A numerical study of island wakes in the Southern California Bight. Cont. Shelf Res. 27 (9), 1233–1248. http://dx.doi.org/10.1016/j.csr.2007.01.016.

Edson, J.B., Jampana, V., Weller, R.A., Bigorre, S.P., Plueddemann, A.J., Fairall, C.W., Miller, S.D., Mahrt, L., Vickers, D., Hersbach, H., 2013. On the exchange of momentum over the open ocean. J. Phys. Oceanogr. 43 (8), 1589–1610. http://dx.doi.org/10.1175/JPO-D-12-0173.1.

Elliot, S., MacDonald, H., Zamnit, C., Hoang, L., 2021. Hauraki Integrated Land-Water Model. Client Report 2021171HN, National Institue of Water and Atmospheric of New Zealand, p. 88, URL: https://niwa.co.nz/sites/niwa.co.nz/files/Hauraki 20land-water 20modelling 20report 2016 20FINAL.pdf.

Fairall, C.W., Bradley, E.F., Godfrey, J.S., Wick, G.A., Edson, J.B., Young, G.S., 1996a. Cool-skin and warm-layer effects on sea surface temperature. J. Geophys. Res.: Oceans 101 (C1), 1295–1308. http://dx.doi.org/10.1029/95JC03190, URL: http://doi.wiley.com/10.1029/95JC03190.

Fairall, C.W., Bradley, E.F., Rogers, D.P., Edson, J.B., Young, G.S., 1996b. Bulk parameterization of air-sea fluxes for Tropical Ocean-Global Atmosphere Coupled-Ocean Atmosphere Response Experiment. J. Geophys. Res.: Oceans 101 (C2), 3747–3764. http://dx.doi.org/10.1029/95JC03205, URL: http://doi.wiley.com/10.1029/95JC03205.

Fernandez, D., Bowen, M., Sutton, P., 2018. Variability, coherence and forcing mechanisms in the New Zealand ocean boundary currents. Prog. Oceanogr. 165, 168–188. http://dx.doi.org/10.1016/j.pocean.2018.06.002.

Goubanova, K., Sanchez-Gomez, E., Frauen, C., Voldoire, A., 2019. Respective roles of remote and local wind stress forcings in the development of warm SST errors in the South-Eastern Tropical Atlantic in a coupled high-resolution model. Clim. Dynam. 52 (3–4), 1359–1382. http://dx.doi.org/10.1007/s00382-018-4197-0.

Hadfield, M.G., Stevens, C.L., 2021. A modelling synthesis of the volume flux through Cook Strait. New Zealand J. Mar. Freshw. Res. 55 (1), 65–93. http://dx.doi.org/10.1080/00288330.2020.1784963.

Haney, R.L., 1991. On the pressure gradient force over steep topography in sigma coordinate ocean models. J. Phys. Oceanogr. 21 (4), 610–619. http://dx.doi.org/10.1175/1520-0485(1991)021<0610:OTPGFO>2.0.CO;2.

Hauri, C., Schultz, C., Hedstrom, K., Danielson, S., Irving, B., Doney, S.C., Dussin, R., Curchitser, E.N., Hill, D.F., Stock, C.A., 2020. A regional hindcast model simulating ecosystem dynamics, inorganic carbon chemistry, and ocean acidification in the Gulf of Alaska. Biogeosciences 17 (14), 3837–3857. http://dx.doi.org/10.5194/bg-17-3837-2020.

Haza, A.C., Poje, A.C., Özgökmen, T.M., Martin, P., 2008. Relative dispersion from a high-Resolution Coastal model of the Adriatic Sea. Ocean Model. 22 (1–2), 48–65. http://dx.doi.org/10.1016/j.ocemod.2008.01.006.

Heath, R.A., 1985. A review of the physical oceanography of the seas around New Zealand — 1982. New Zealand J. Mar. Freshw. Res. 19 (1), 79–124. http://dx.doi.org/10.1080/00288330.1985.9516077.

Janeković, I., Powell, B., 2012. Analysis of imposing tidal dynamics to nested numerical models. Cont. Shelf Res. 34, 30–40. http://dx.doi.org/10.1016/j.csr.2011.11.017.

Jones, H., Poot, M., Mullarney, J., de Lange, W., Bryan, K., 2016. Oil dispersal modelling: Reanalysis of the *Rena* oil spill using open-source modelling tools. New Zealand J. Mar. Freshw. Res. 50 (1), 10–27. http://dx.doi.org/10.1080/00288330.2015.1112819.

Kärnä, T., Baptista, A.M., Lopez, J.E., Turner, P.J., McNeil, C., Sanford, T.B., 2015. Numerical modeling of circulation in high-energy estuaries: A Columbia River estuary benchmark. Ocean Model. 88, 54–71. http://dx.doi.org/10.1016/j.ocemod.2015.01.001.

LaCasce, J., 2008. Statistics from Lagrangian observations. Prog. Oceanogr. 77 (1), 1–29. http://dx.doi.org/10.1016/j.pocean.2008.02.002.

LaCasce, J.H., Ohlmann, C., 2003. Relative dispersion at the surface of the Gulf of Mexico. J. Mar. Res. 61 (3), 285–312. http://dx.doi.org/10.1357/002224003322201205.

Largier, J.L., 2020. Upwelling bays: How Coastal upwelling controls circulation, habitat, and productivity in bays. Ann. Rev. Mar. Sci. 12 (1), 415–447. http://dx.doi.org/10.1146/annurev-marine-010419-011020.

Liu, Y., MacCready, P., Hickey, B.M., Dever, E.P., Kosro, P.M., Banas, N.S., 2009. Evaluation of a coastal ocean circulation model for the Columbia River plume in summer 2004. J. Geophys. Res. 114, C00B04. http://dx.doi.org/10.1029/2008JC004929.

Longdill, P.C., 2008. Environmentally Sustainable Aquaculture: An Eco-Physical Perspective (Ph.D. thesis). University of Waikato, Hamilton, New Zealand, URL: https://hdl.handle.net/10289/2604.

Longdill, P.C., Healy, T.R., Black, K.P., 2008. Transient wind-driven coastal upwelling on a shelf with varying width and orientation. New Zealand J. Mar. Freshw. Res. 42 (2), 181–196. http://dx.doi.org/10.1080/00288330809509947.

Ludovic, B., Byron, B., Christopher, F., Elizabeth, T., Jim, E., Robert, P., 2021. Python Implementation of the COARE 3.5 Bulk Air-Sea Flux Algorithm. Zenodo, http://dx.doi.org/10.5281/ZENODO.5110991, URL: https://zenodo.org/record/5110991.

Mason, E., Molemaker, J., Shchepetkin, A.F., Colas, F., McWilliams, J.C., Sangrà, P., 2010. Procedures for offline grid nesting in regional ocean models. Ocean Model. 35 (1–2), 1–15. http://dx.doi.org/10.1016/j.ocemod.2010.05.007.

Mitarai, S., Siegel, D.A., Watson, J.R., Dong, C., McWilliams, J.C., 2009. Quantifying connectivity in the coastal ocean with application to the Southern California Bight. J. Geophys. Res. 114 (C10), C10026. http://dx.doi.org/10.1029/2008JC005166.

Mitchell, J., Mackay, K., Neil, H., Pallentin, A., Notman, P., 2012. Undersea New Zealand, 1:5,000,000. NIWA Chart, Miscellaneous Series, No. 92, National Institue of Water and Atmospheric of New Zealand, URL: https://niwa.co.nz/our-science/oceans/bathymetry/further-information.

Myksvoll, M., Sandvik, A., Skarðhamar, J., Sundby, S., 2012. Importance of high resolution wind forcing on eddy activity and particle dispersion in a Norwegian fjord. Estuar. Coast. Shelf Sci. 113, 293–304. http://dx.doi.org/10.1016/j.ecss.2012.08.019.

NIWA, 2022. Historic Weather Events Catalog. Catalog, National Institue of Water and Atmospheric of New Zealand, URL: www.hwe.niwa.co.nz.

Norrie, C., Dunphy, B., Roughan, M., Weppe, S., Lundquist, C., 2020. Spill-over from aquaculture may provide a larval subsidy for the restoration of mussel reefs. Aquac. Environ. Interact. 12, 231–249. http://dx.doi.org/10.3354/aei00363.

Pawlowicz, R., Beardsley, B., Lentz, S., 2002. Classical tidal harmonic analysis including error estimates in MATLAB using T_TIDE. Comput. Geosci. 28 (8), 929–937. http://dx.doi.org/10.1016/S0098-3004(02)00013-4.

Ridgway, K., Dunn, J., 2003. Mesoscale structure of the mean East Australian Current System and its relationship with topography. Prog. Oceanogr. 56 (2), 189–222. http://dx.doi.org/10.1016/S0079-6611(03)00004-1.

Ridgway, N.M., Greig, M.J.N., 1986. Water movements in bay of plenty, New Zealand. New Zealand J. Mar. Freshw. Res. 20 (3), 447–453. http://dx.doi.org/10.1080/00288330.1986.9516164.

Roemmich, D., Sutton, P., 1998. The mean and variability of ocean circulation past northern New Zealand: Determining the representativeness of hydrographic climatologies. J. Geophys. Res.: Oceans 103 (C6), 13041–13054. http://dx.doi.org/10.1029/98JC00583.

Romero, L., Uchiyama, Y., Ohlmann, J.C., McWilliams, J.C., Siegel, D.A., 2013. Simulations of nearshore particle-pair dispersion in Southern California. J. Phys. Oceanogr. 43 (9), 1862–1879. http://dx.doi.org/10.1175/JPO-D-13-011.1.

Roughan, M., Mace, A., Largier, J.L., Morgan, S., Fisher, J., Carter, M., 2005. Subsurface recirculation and larval retention in the lee of a small headland: A variation on the upwelling shadow theme. J. Geophys. Res. 110 (C10), C10027. http://dx.doi.org/10.1029/2005JC002898.

Roughan, M., Schaeffer, A., Suthers, I.M., 2015. Sustained ocean observing along the coast of Southeastern Australia. In: Coastal Ocean Observing Systems. Elsevier, pp. 76–98. http://dx.doi.org/10.1016/B978-0-12-802022-7.00006-7.

Sansón, L.Z., Pérez-Brunius, P., Sheinbaum, J., 2017. Surface relative dispersion in the Southwestern Gulf of Mexico. J. Phys. Oceanogr. 47 (2), 387–403. http://dx.doi.org/10.1175/JPO-D-16-0105.1.

Santana, R., Suanda, S.H., Macdonald, H., O'Callaghan, J., 2021. Mesoscale and wind-driven intra-annual variability in the East Auckland Current. Sci. Rep. 11 (1), 9764. http://dx.doi.org/10.1038/s41598-021-89222-3, URL: http://www.nature.com/articles/s41598-021-89222-3.

Sharples, J., Greig, M.J.N., 1998. Tidal currents, mean flows, and upwelling on the north-east shelf of New Zealand. New Zealand J. Mar. Freshw. Res. 32 (2), 215–231. http://dx.doi.org/10.1080/00288330.1998.9516821.

Shchepetkin, A.F., McWilliams, J.C., 2003. A method for computing horizontal pressure-gradient force in an oceanic model with a nonaligned vertical coordinate. J. Geophys. Res. 108 (C3), 3090. http://dx.doi.org/10.1029/2001JC001047.

Shchepetkin, A.F., McWilliams, J.C., 2005. The regional oceanic modeling system (ROMS): A split-explicit, free-surface, topography-following-coordinate oceanic model. Ocean Model. 9 (4), 347–404. http://dx.doi.org/10.1016/j.ocemod.2004.08.002.

Sikirić, M.D., Janeković, I., Kuzmić, M., 2009. A new approach to bathymetry smoothing in sigma-coordinate ocean models. Ocean Model. 29 (2), 128–136. http://dx.doi.org/10.1016/j.ocemod.2009.03.009.

Silva, C.N.S., Macdonald, H.S., Hadfield, M.G., Cryer, M., Gardner, J.P.A., 2019. Ocean currents predict fine-scale genetic structure and source-sink dynamics in a marine Invertebrate Coastal Fishery. ICES J. Mar. Sci. 76 (4), 1007–1018. http://dx.doi.org/10.1093/icesjms/fsy201, URL: https://academic.oup.com/icesjms/article/76/4/1007/5303700.

Solano, M., Canals, M., Leonardi, S., 2020. Barotropic boundary conditions and tide forcing in split-explicit high Resolution Coastal ocean models. J. Ocean Eng. Sci. 5 (3), 249–260. http://dx.doi.org/10.1016/j.joes.2019.12.002.

Souza, J.M.A.C., 2022. Moana ocean hindcast. http://dx.doi.org/10.5281/ZENODO.5895265.

Souza, J.M.A.C., Powell, B., Castillo-Trujillo, A.C., Flament, P., 2015. The vorticity balance of the ocean surface in Hawaii from a regional reanalysis. J. Phys. Oceanogr. 45 (2), 424–440. http://dx.doi.org/10.1175/JPO-D-14-0074.1.

Souza, J.M.A.C., Suanda, S.H., Couto, P.P., Smith, R.O., Kerry, C., Roughan, M., 2022. Moana ocean hindcast – a 25+ years simulation for New Zealand Waters using the ROMS v3.9 model. http://dx.doi.org/10.5194/egusphere-2022-41, EGUsphere [Pre-Print].

Stanton, B.R., Sutton, P.J.H., 2003. Velocity measurements in the East Auckland Current north-east of North Cape, New Zealand. New Zealand J. Mar. Freshw. Res. 37 (1), 195–204. http://dx.doi.org/10.1080/00288330.2003.9517157.

Stanton, B.R., Sutton, P.J.H., Chiswell, S.M., 1997. The East Auckland Current, 1994–95. New Zealand J. Mar. Freshw. Res. 31 (4), 537–549. http://dx.doi.org/10.1080/00288330.1997.9516787.

Stevens, C.L., O'Callaghan, J.M., Chiswell, S.M., Hadfield, M.G., 2021. Physical oceanography of New Zealand/Aotearoa shelf seas – a review. New Zealand J. Mar. Freshw. Res. 55 (1), 6–45. http://dx.doi.org/10.1080/00288330.2019.1588746.

Taylor, G., 1921. Diffusion by continuous movements. Proc. Lond. Math. Soc. 20, 196–212.

Taylor, K.E., 2001. Summarizing multiple aspects of model performance in a single diagram. J. Geophys. Res.: Atmos. 106 (D7), 7183–7192. http://dx.doi.org/10.1029/2000JD900719.

Tilburg, C.E., Hurlburt, H.E., O'Brien, J.J., Shriver, J.F., 2001. The dynamics of the east Australian current system: The tasman front, the east auckland current, and the east cape current. J. Phys. Oceanogr. 31 (10), 2917–2943. http://dx.doi.org/10.1175/1520-0485(2001)031<2917:TDOTEA>2.0.CO;2.

Warner, J.C., Geyer, W.R., Lerczak, J.A., 2005. Numerical modeling of an estuary: A comprehensive skill assessment. J. Geophys. Res. 110 (C5), C05001. http://dx.doi.org/10.1029/2004JC002691.

Wilkin, J.L., 2006. The summertime heat budget and circulation of southeast new England shelf waters. J. Phys. Oceanogr. 36 (11), 1997–2011. http://dx.doi.org/10.1175/JPO2968.1.

Willmott, C.J., 1981. On the validation of models. Phys. Geogr. 2 (2), 184–194. http://dx.doi.org/10.1080/02723646.1981.10642213.

Wing, S.R., Botsford, L., Largier, J.L., Morgan, L., 1995. Spatial structure of relaxation events and crab settlement in the northern California upwelling system. Mar. Ecol. Prog. Ser. 128, 199–211. http://dx.doi.org/10.3354/meps128199.

Zeldis, J.R., Walters, R.A., Greig, M.J., Image, K., 2004. Circulation over the northeastern New Zealand continental slope, shelf and adjacent Hauraki Gulf, during spring and summer. Cont. Shelf Res. 24 (4–5), 543–561. http://dx.doi.org/10.1016/j.csr.2003.11.007.

Zhang, H., Cheng, W., Chen, Y., Shi, Z., Gong, W., Liu, S., 2019. Importance of large-Scale Coastal circulation on bay-shelf exchange and residence time in a subtropical embayment, the northern South China Sea. Ocean Coastal Manag 168, 72–89. http://dx.doi.org/10.1016/j.ocecoaman.2018.10.033.